DEPARTMENT OF PHYSICS
UNIVERSITY OF JYVÄSKYLÄ
RESEARCH REPORT No. 7/2006

APPLICATION OF THE LATTICE-BOLTZMANN METHOD TO MULTIPHASE FLOWS

BY
JARI HYVÄLUOMA

Academic Dissertation
for the Degree of
Doctor of Philosophy

To be presented, by permission of the
Faculty of Mathematics and Science
of the University of Jyväskylä,
for public examination in Auditorium FYS-1 of the
University of Jyväskylä on June 22, 2006
at 12 o'clock noon

Jyväskylä, Finland
June, 2006

ISBN 978-951-39-3172-8
URN:ISBN:978-951-39-3172-8

Preface

The work reviewed in this thesis has been carried out during the years 2002-2006 in the Department of Physics at the University of Jyväskylä.

First I would like to thank my supervisors Jussi Timonen and Markku Kataja for their competent guidance in all stages of this work and for the opportunity to work in their group. I would also like to express my deep gratitude to Pasi Raiskinmäki for his invaluable help and advice and for continuous encouragement. I wish to thank Antti Koponen, Ari Jäsberg, and Tuomas Turpeinen for their important contributions to the enclosed articles, and Keijo Mattila for a fruitful collaboration and many inspiring discussions. Special thanks are due to Juha Merikoski for his help, especially during the years 2001-2002.

I am grateful to the whole staff of the department for an inspiring working atmosphere. I thank the people in FL348, especially Janne Juntunen, Tomi Kemppinen, Viivi Koivu, and Lasse Miettinen, for coffee, company, and collaboration.

The financial support from TEKES and University of Jyväskylä is gratefully acknowledged.

Finally I thank my parents and my brother and his family for their support.

Jyväskylä, June 2006

Jari Hyväluoma

Abstract

This work deals with multiphase fluids which are investigated numerically with the lattice-Boltzmann method. Two multiphase systems were studied, namely liquid-vapour flow in paper and shear flow of a non-colloidal and non-Brownian liquid-particle suspension.

We simulated the behaviour of liquids in an X-ray tomographic reconstruction of a sample of paper board. For a wetting liquid we considered three different types of capillary penetration processes, unidirectional and radial penetration of the liquid, as well as penetration of a small liquid droplet in the paper sample. Results obtained for unidirectional penetration could well be described with the Lucas–Washburn equation and those for radial penetration using a capillary model for such penetration process. Also the data obtained from the droplet penetration were in qualitative agreement with a generalised radial penetration equation. We also studied intrusion of a non-wetting liquid into the paper. Our results were in good agreement with those obtained from experiments when the simulated data were interpreted exactly as in pore-size distribution measurements with mercury-intrusion porosimetry. However, a different result was found by image analysis. This deviation was found to result from the 'ink-bottle' effect which is a consequence of not having equal access to all pores in the sample.

For the liquid-particle suspensions we analysed the effect of particle clusters on the viscosity of the suspension. Detailed momentum-transfer analysis was carried out for simple suspensions with a single particle or with a single chainlike cluster, as well as for suspensions with thousands of particles. Our analyses showed how clusters contribute to the viscosity of suspensions by acting as channels for momentum transfer. We investigated in particular the so-called strain-hardening phenomenon, and showed that it can be explained by formation of particle clusters.

Keywords: lattice-Boltzmann method, multiphase flows, imbibition, mercury-intrusion porosimetry, liquid-particle suspensions, strain hardening.

Author's address Jari Hyväluoma
Department of Physics
University of Jyväskylä
Finland

Supervisors Professor Jussi Timonen
Department of Physics
University of Jyväskylä
Finland

Professor Markku Kataja
Department of Physics
University of Jyväskylä
Finland

Doctor Pasi Raiskinmäki
Department of Physics
University of Jyväskylä
Finland

Reviewers Academy Professor Risto Nieminen
Laboratory of Physics
Helsinki University of Technology
Finland

Doctor Kevin Stratford
Edinburgh Parallel Computing Centre
The University of Edinburgh
UK

Opponent Professor Joel Koplik
Levich Institute
The City University of New York
USA

List of Publications

I J. Hyväluoma, P. Raiskinmäki, A. Jäsberg, A. Koponen, M. Kataja, and J. Timonen, *Simulation of liquid penetration in paper*, Physical Review E **73**, 036705 (2006).

II J. Hyväluoma, P. Raiskinmäki, A. Jäsberg, A. Koponen, M. Kataja, and J. Timonen, *Evaluation of a lattice-Boltzmann method for mercury intrusion porosimetry simulations*, Future Generation Computer Systems **20**, 1003-1011 (2004).

III J. Hyväluoma, T. Turpeinen, P. Raiskinmäki, A. Jäsberg, A. Koponen, M. Kataja, J. Timonen, and S. Ramaswamy, *Intrusion of non-wetting liquid in paper*, submitted for publication.

IV J. Hyväluoma, P. Raiskinmäki, A. Koponen, M. Kataja, and J. Timonen, *Lattice-Boltzmann simulation of particle suspensions in shear flow*, Journal of Statistical Physics **121**, 149-161 (2005).

V J. Hyväluoma, P. Raiskinmäki, A. Koponen, M. Kataja, and J. Timonen, *Strain hardening in liquid-particle suspensions*, Physical Review E **72**, 061402 (2005).

The author of this thesis performed all lattice-Boltzmann simulations reported in articles I-V and wrote the first drafts of the articles.

Contents

1 Introduction

Multiphase fluids are substances that include matter in different phases in coexistence, and the resulting substance has a fluid-like behaviour. Dynamics of multiphase flows is more complicated than that of single-phase flows. Their behaviour depends not only on the macroscopic conservation laws but also on the interactions between different substances in the system. Even more complicated phenomena are present in so-called complex multiphase flows such as reactive flows, magnetic flows, and flows with electric charges.

One specific type of multiphase flows is composed of flows where the flowing substance is a mixture of several different liquids or where liquid and gas phases coexist. Examples of these flows include, e.g., oil-water systems, bubble flows, breaking of liquid jets, sprays, spreading and sliding droplets on solid surfaces, and imbibition of liquids in porous structures. Further, the last of these examples includes many interesting phenomena which are important from an industrial and thereby also from an economical point of view, but as well from a scientific point of view. Dynamics of wetting liquid fronts in porous media is one of the long-lasting problems in statistical physics. On the other hand, non-wetting liquids have been used to characterise the pore structure of materials for more than a half of a century using mercury-intrusion porosimetry. The validity of this method is still, however, a fairly open question. Also, penetration of liquid drops into porous structures has many important applications such as paper coating or ink-jet printing, just to mention two examples.

Another type of multiphase fluid present in many processes is the fluid-particle suspension. One suspension of special importance is the blood. Blood consists of many types of cells such as leukocytes, erythocytes, and platelets suspended in the blood plasma. Suspensions are also commonly met in many branches of industry. For example, gas-particle suspensions are present in many processes in chemical engineering, and liquid-particle suspensions in printing and coating technologies.

The behaviour of multiphase flows is still largely unknown. Multiphase flow research has traditionally been done with help of experiments and by theoretical calculations and models. In theoretical models multiphase fluids are often described using a continuum approach where the mesoscopic character of the fluid is ignored and the effect of different phases is hidden in the constitutive relations. Although this kind approach may be helpful in solving engineering problems, it does not

clarify the underlying mechanism responsible for the non-Newtonian behaviour of the fluid. On the other hand, it is possible to measure rheological properties of multiphase fluids, but the experimental verification of the underlying phenomena responsible for these properties has turned out to be a difficult task.

During the last two decades computer simulations have become an important tool in the quest to understand the physical mechanisms responsible for the complex behaviour of multiphase flows. In liquid-particle suspensions, for example, simulations form an excellent tool to study the particle-scale mechanisms that significantly alter the macroscopic behaviour of the suspension. In simulations, one can model the suspension on a level where individual particles and their interactions with fluid and each others are taken into account. Therefore, they can provide detailed information of the structural features that affect the rheological behaviour of the suspension at larger scales.

The specific numerical simulation tool used in the investigations reported in this Thesis is the lattice-Boltzmann method. This method was developed from the lattice-gas cellular automata. As the lattice-Boltzmann method produces in the hydrodynamic limit a flow field obeying the Navier–Stokes equation, it is a decent method for fluid-flow simulations. Partly owing to its intuitively clear dynamics inherited from the lattice gases, the lattice-Boltzmann method has been particularly successful in modelling multiphase flows and flow in materials with complex internal structure. Later also a more rigorous physical background and mathematical connection to kinetic theory have been established.

In this Thesis we use the lattice-Boltzmann method to study two types of multiphase flows. These flows are liquid-vapour flow in porous media and shear flow of a non-colloidal and non-Brownian liquid-particle suspension. Using the Shan–Chen multiphase model for vapour-liquid flows within the lattice-Boltzmann method, we simulated behaviour of both wetting and non-wetting liquids in paper. As a geometry for the simulation we used a high-resolution X-ray tomographic image of a paper sample. We found that the lattice-Boltzmann method is able to produce results that agree very well with experimentally verified capillary models developed for penetration of wetting liquids in porous materials. Using a non-wetting liquid we analysed the operation of mercury-intrusion porosimetry. We found that assumptions used when interpretating data in mercury-intrusion porosimetry are not valid in paper, and we believe that this is the case also more generally. For the non-colloidal and non-Brownian liquid-particle suspension, we considered the momentum-transfer mechanisms responsible for the enhanced viscosity observed in measurements on suspensions of this kind. The main emphasis was on the strain-hardening effect which is observed in many rheological materials including liquid-particle suspensions. We were able to show that formation of stress-bearing particle clusters is the mechanism behind strain hardening in suspensions.

The outline of this Thesis is as follows. We start by reviewing some aspects of classical kinetic theory and the lattice-Boltzmann method. We discuss the connection between the continuum-limit Boltzmann equation and the lattice-Boltzmann equation, and describe the multiphase models used with the lattice-Boltzmann method. In Chapter 4 we review some capillary models that are used to describe the behaviour of liquids in porous materials, and present results from the liquid-vapour simulations using both wetting and non-wetting liquid. After this, in Chapter 5, we describe properties of liquid-particle suspensions and present results from the simulations. Finally in the last Chapter, we summarise the results and give some concluding remarks.

2 Fluid mechanics and classical kinetic theory

2.1 Fluid mechanics

As fluids we understand such substances that deform continuously under stress. Most common fluids include liquids and gases, which are often referred to as simple fluids. So-called complex fluids include, e.g., mixtures of liquids and gases, fluids containing solid particles, and foams. In this Section we consider only simple fluids and return to more complex cases later.

Since fluids consist of molecules, an accurate description of motion of fluids would be given by molecular dynamics where fluid is treated as a collection of a large number of interacting molecules, and all molecular-level interactions are taken into account. Although this approach might be adequate in some applications in micro- and nanofluidics, in most cases molecular dynamics is computationally much too expensive to be used in solving practical fluid-flow problems, since the number of molecules in realistic systems is typically of order 10^{23}. However, in most cases such a microscopic approach includes a lot of information which is unimportant and is not needed for understanding flow situations in engineering problems. Therefore, a less accurate description of fluid turns out be satisfactory, and usually fluid is treated as a continuum.

In a continuum approach, instead of tracking positions and velocities of individual particles, motion of fluid is described in terms of averaged quantities such as density, pressure and velocity. To be well defined, such quantities need to be averaged over a control volume which is large enough to include a large number of particles but small enough compared to the macroscopic length scale, so that variations in fluid properties are observed. These requirements are easily fulfilled in typical engineering fluid-flow problems.

The governing principles under flow equations are conservation of mass and Newton's second law [1]. Conservation of mass is described by the continuity equation

$$\partial_t \rho + \partial_\alpha (\rho u_\alpha) = 0, \tag{2.1}$$

in which ρ is the density of fluid and $\mathbf{u}$ is its velocity. Newton's second law leads

to the momentum equation

$$f_\alpha = \frac{\mathrm{d}(\rho u_\alpha)}{\mathrm{d}t} = \partial_t(\rho u_\alpha) + \partial_\beta \Pi_{\alpha\beta}, \tag{2.2}$$

where $\mathbf{f}$ is the density of the external forces acting on the fluid and $\Pi_{\alpha\beta}$ is the momentum-flux tensor that gives the flux of the α component of the momentum in the β direction. If there is no external force, the momentum equation stands for the principle of conservation of momentum. In the case of incompressible fluids, Eqs. (2.1) and (2.2) are reduced to

$$\partial_\alpha u_\alpha = 0 \tag{2.3}$$

and

$$f_\alpha = \rho \partial_t u_\alpha + \partial_\beta \Pi_{\alpha\beta}. \tag{2.4}$$

In this Thesis we consider only incompressible fluids. For thermal flows one needs in addition an energy equation, resulting from the conservation of energy. However, we consider only isothermal flows and the energy equation is thus ignored.

The momentum equation can be written in a more convenient form by using a detailed expression for the momentum-flux tensor. Generally the momentum-flux tensor can be written as

$$\Pi_{\alpha\beta} = \rho u_\alpha u_\beta - \sigma_{\alpha\beta}, \tag{2.5}$$

where the first term on the right-hand side describes the convective momentum flux, and $\sigma_{\alpha\beta}$ is the stress tensor of the fluid. Stress tensor can be further divided in two parts,

$$\sigma_{\alpha\beta} = -p\delta_{\alpha\beta} + \sigma'_{\alpha\beta}. \tag{2.6}$$

Here pressure p is the isotropic part of the stress tensor and $\sigma'_{\alpha\beta}$ is the deviatoric (or viscous) stress tensor. For Newtonian and isotropic fluids deviatoric stresses are given by the constitutive equation

$$\sigma'_{\alpha\beta} = \mu \left(\partial_\alpha u_\beta + \partial_\beta u_\alpha \right). \tag{2.7}$$

Here the proportionality coefficient μ between stress and shear rate is the dynamic shear viscosity. By substituting the obtained momentum-flux tensor in the momentum equation, we obtain the Navier–Stokes equation

$$\partial_t u_\alpha + u_\beta \partial_\beta u_\alpha = -\frac{1}{\rho}\partial_\alpha p + \frac{\mu}{\rho}\partial^2_{\beta\beta} u_\alpha + \frac{1}{\rho} f_\alpha. \tag{2.8}$$

Navier–Stokes equation is a second-order nonlinear partial differential equation and it can be solved analytically only under some special circumstances. In some cases it can be sufficient to use restricted forms of the momentum flux tensor and

of the momentum equation thus obtained. For example, when the convective momentum flux is small compared to the viscous stress, the convective mometum flux can be neglected. The momentum equation is now reduced to the Stokes equation

$$\partial_t u_\alpha = -\frac{1}{\rho}\partial_\alpha p + \frac{\mu}{\rho}\partial^2_{\beta\beta} u_\alpha + \frac{1}{\rho} f_\alpha. \tag{2.9}$$

As an analytical solution for the Navier–Stokes equation is in most cases unknown, numerical methods are often used when studying flow problems. The 'conventional' approach in computational fluid dynamics is to discretise the Navier–Stokes equation, and to numerically solve the discrete equation thus obtained using the relevant initial and boundary conditions. Well-known methods in computational fluid dynamics following this path include, e.g., the finite-difference, finite-volume, and finite-element methods. Another possibility is to use particle-based methods such as lattice-gas cellular automata [2], dissipative particle dynamics [3], or smoothed particle dynamics [4]. Lattice-Boltzmann method has been compared to some other numerical methods by Nourgaliev et al. with a special emphasis on multiphase flows [5].

2.2 The BBGKY hierarchy

In kinetic theory, properties of the fluid are described by using a distribution function rather than considering each of the molecules separately. Let us consider an ensemble of systems with N identical point particles with mass m [6]. Each particle has three translational degrees of freedom. At a certain time t, the state of this system can be described as a point in a $6N$-dimensional phase space spanned by $3N$ coordinates $\mathbf{r}^N = \{\mathbf{r}_1, \mathbf{r}_2, \ldots, \mathbf{r}_N\}$ and $3N$ momenta $\mathbf{p}^N = \{\mathbf{p}_1, \mathbf{p}_2, \ldots, \mathbf{p}_N\}$. Since all particles have the same mass, the momenta of the particles can be written as $\mathbf{p}^N = m\boldsymbol{\xi}^N$, where $\boldsymbol{\xi}^N = \{\boldsymbol{\xi}_1, \boldsymbol{\xi}_2, \ldots, \boldsymbol{\xi}_N\}$ stands for the microscopic velocities of the particles. The Hamiltonian of this system can be written as

$$\mathcal{H}_N\left(\mathbf{r}^N, \boldsymbol{\xi}^N\right) = \frac{1}{2} m \sum_{i=1}^{N} \boldsymbol{\xi}^2 + V_N(\mathbf{r}^N), \tag{2.10}$$

where V_N is the total potential energy of the system. Time evolution of the system is given by the Hamilton's equations

$$\frac{\mathrm{d}\mathbf{r}_i}{\mathrm{d}t} = \nabla_{\mathbf{p}_i} \mathcal{H}_N, \tag{2.11}$$

$$\frac{\mathrm{d}\mathbf{p}_i}{\mathrm{d}t} = -\nabla_{\mathbf{r}_i} \mathcal{H}_N, (i = 1, 2, \ldots, N). \tag{2.12}$$

Distribution of the phase-space points is given by the N-particle distribution function $f^{(N)}\left(\mathbf{r}^N, \boldsymbol{\xi}^N; t\right)$. The probability that the system at time t is in a microscopic state described by a infinitesimal $6N$-dimensional phase-space element $\mathrm{d}\mathbf{r}^N \mathrm{d}\boldsymbol{\xi}^N$ is given by $f^{(N)}\left(\mathbf{r}^N, \boldsymbol{\xi}^N; t\right) \mathrm{d}\mathbf{r}^N \mathrm{d}\boldsymbol{\xi}^N$. It is evident that integral of the distribution function over all coordinates and momenta is constant. This fact is reflected in the Liouville equation which gives the time evolution of the distribution function,

$$\frac{\partial f^{(N)}}{\partial t} = \frac{1}{m} \sum_{i=1}^{N} \left(\nabla_{\mathbf{r}_i} \mathcal{H}_N \cdot \nabla_{\boldsymbol{\xi}_i} f^N - \nabla_{\boldsymbol{\xi}_i} \mathcal{H}_N \cdot \nabla_{\mathbf{r}_i} f^N \right). \tag{2.13}$$

Liouville equation is nothing but a $6N$-dimensional version of the continuity equation, in which Hamiltonian mechanics is included via Eqs. (2.11) and (2.12).

If the only forces acting on particle i are the external force $\mathbf{X}_i$ and the pairwise interaction forces $\mathbf{F}_{ij}$ due to the other particles j ($\mathbf{F}_{ii} = 0$), Liouville equation can be written in the form

$$\frac{\partial f^{(N)}}{\partial t} + \sum_{i=1}^{N} \boldsymbol{\xi}_i \cdot \nabla_{\mathbf{r}_i} f^{(N)} + \frac{1}{m} \sum_{i=1}^{N} \mathbf{X}_i \cdot \nabla_{\boldsymbol{\xi}_i} f^{(N)} = -\frac{1}{m} \sum_{i=1}^{N} \sum_{j=1}^{N} \mathbf{F}_{ij} \cdot \nabla_{\boldsymbol{\xi}_i} f^{(N)}. \tag{2.14}$$

Next we consider such a case where only a subset of $n(< N)$ particles is of interest. Additional information can be removed by integrating $f^{(N)}$ over the positions and momenta of the other $(N - n)$ particles. This leads to an n-particle distribution function

$$f^{(n)}\left(\mathbf{r}^n, \boldsymbol{\xi}^n; t\right) = \frac{N!}{(N-n)!} \int \mathrm{d}\mathbf{r}^{N-n} \int \mathrm{d}\boldsymbol{\xi}^{N-n} f^{(N)}\left(\mathbf{r}^N, \boldsymbol{\xi}^N; t\right), \tag{2.15}$$

where we have used notation $\mathbf{r}^{(n)} = \{\mathbf{r}_1, \ldots, \mathbf{r}_n\}$, $\mathbf{r}^{(N-n)} = \{\mathbf{r}_{n+1}, \ldots, \mathbf{r}_N\}$, etc. Defining $f^{(n)}$ in this way, $f^{(n)} \mathrm{d}\mathbf{r}^n \mathrm{d}\mathbf{p}^n$ is $N!/(N-n)!$ times the probability of finding any subset of n particles in the reduced phase-space element $\mathrm{d}\mathbf{r}^n \mathrm{d}\mathbf{p}^n$ at time t no matter what the positions and momenta of the remaining particles are. Also Liouville equation (Eq. (2.14)) can be integrated over these $6(N-n)$ uninteresting degrees of freedom. By noticing that $f^{(N)}$ is symmetric with respect to changes of indices, we obtain an equation connecting $f^{(n)}$ and $f^{(n+1)}$,

$$\begin{aligned} &\left\{ \frac{\partial}{\partial t} + \sum_{i=1}^{n} \left[\boldsymbol{\xi}_i \cdot \nabla_{\mathbf{r}_i} + \frac{1}{m} \left(\mathbf{X}_i + \sum_{j=1}^{n} \mathbf{F}_{ij} \right) \cdot \nabla_{\boldsymbol{\xi}_i} \right] \right\} f^{(n)}\left(\mathbf{r}^n, \boldsymbol{\xi}^n; t\right) \\ &\quad = -\frac{1}{m} \sum_{i=1}^{n} \int \mathrm{d}\mathbf{r}_{n+1} \int \mathrm{d}\boldsymbol{\xi}_{n+1} \mathbf{F}_{i,n+1} \cdot \nabla_{\boldsymbol{\xi}_i} f^{(n+1)}\left(\mathbf{r}^{n+1}, \boldsymbol{\xi}^{n+1}; t\right). \end{aligned} \tag{2.16}$$

This famous set of equation for $n = 1, 2, \ldots, N-1$ is known as the BBGKY hierarchy after Bogolyubov, Born, Green, Kirkwood, and Yvon. However, this type of

equation alone is not useful since it expresses an unknown distribution function $f^{(n)}$ in terms of another unknown distribution function $f^{(n+1)}$. Some additional assumptions are needed to close this set of equations.

2.3 The Boltzmann equation

Boltzmann equation describes a system consisting of a dilute gas with high enough temperature and low enough density so that the molecules of the gas can be considered to move freely and interacting with each other only while colliding. In other words, the potential energy of the interaction is negligible compared to the kinetic energy of the motion.

In the previous Section we derived a set of kinetic equations, Eq. (2.16). For practical purposes, the most important kinetic equation is obtained by selecting $n = 1$ in Eq. (2.16). In this case we obtain

$$\left(\frac{\partial}{\partial t} + \boldsymbol{\xi}_1 \cdot \nabla_{\mathbf{r}_1} + \frac{1}{m}\mathbf{X}_1 \cdot \nabla_{\boldsymbol{\xi}_i}\right) f^{(1)}\left(\mathbf{r}_1, \boldsymbol{\xi}_1; t\right) = -\int \mathrm{d}\mathbf{r}_2 \int \mathrm{d}\mathbf{p}_2 \mathbf{F}_{12} \cdot \nabla_{\mathbf{p}_1} f^{(2)}\left(\mathbf{r}_1, \boldsymbol{\xi}_1, \mathbf{r}_2, \boldsymbol{\xi}_2; t\right) \tag{2.17}$$

The single-particle distribution function $f^{(1)}$ and the two-particle distribution function $f^{(2)}$ are such that $f^{(1)}\mathrm{d}\mathbf{r}_1\mathrm{d}\boldsymbol{\xi}_1$ is N times the probability of finding a particle in the phase-space element $\mathrm{d}\mathbf{r}_1\mathrm{d}\boldsymbol{\xi}_1$, and $f^{(2)}\mathrm{d}\mathbf{r}_1\mathrm{d}\boldsymbol{\xi}_1\mathrm{d}\mathbf{r}_2\mathrm{d}\boldsymbol{\xi}_2$ is $N(N-1)$ times the probability of finding one particle in element $\mathrm{d}\mathbf{r}_1\mathrm{d}\boldsymbol{\xi}_1$ and another one at the same time in element $\mathrm{d}\mathbf{r}_2\mathrm{d}\boldsymbol{\xi}_2$. Thus the number of particles in the system is

$$N = \int f^{(1)}(\mathbf{r}, \boldsymbol{\xi}; t)\mathrm{d}\mathbf{r}\mathrm{d}\boldsymbol{\xi}. \tag{2.18}$$

Also fluid density, momentum density, and energy are obtained from the single-particle distribution function,

$$\rho(\mathbf{r}, t) = \int m f^{(1)}(\mathbf{r}, \boldsymbol{\xi}; t)\mathrm{d}\boldsymbol{\xi} \tag{2.19}$$

$$\rho(\mathbf{r}, t)\mathbf{u}(\mathbf{r}, t) = \int m\boldsymbol{\xi} f^{(1)}(\mathbf{r}, \boldsymbol{\xi}; t)\mathrm{d}\boldsymbol{\xi} \tag{2.20}$$

$$\rho(\mathbf{r}, t)e(\mathbf{r}, t) = \frac{1}{2}\int m(\mathbf{u} - \boldsymbol{\xi})^2 f^{(1)}(\mathbf{r}, \boldsymbol{\xi}; t)\mathrm{d}\boldsymbol{\xi}. \tag{2.21}$$

Here $\mathbf{u}$ is the fluid velocity.

The most famous kinetic equation, the Boltzmann equation, is obtained from Eq. (2.17) under the assumptions that all collisions are binary collisions, the external force has no effect on the cross section of these collisions, and that successive collisions are uncorrelated (molecular chaos). Boltzmann equation is usually written in the form

$$\left(\frac{\partial}{\partial t} + \boldsymbol{\xi} \cdot \nabla + \frac{\mathbf{F}}{m} \cdot \nabla_{\boldsymbol{\xi}}\right) f(\mathbf{r}, \boldsymbol{\xi}, t) = \left(\frac{\partial f}{\partial t}\right)_{\text{coll}}, \tag{2.22}$$

where the collision integral on the right-hand side of the equation describes the effect of particle collisions on the distribution function. An explicit form for the collision integral is given by [7,8]

$$\left(\frac{\partial f}{\partial t}\right)_{\text{coll}} = \int \mathrm{d}\Omega \int \mathrm{d}\boldsymbol{\xi}_* \sigma(\Omega) |\boldsymbol{\xi} - \boldsymbol{\xi}_*| (f'_* f' - f_* f), \tag{2.23}$$

when we assume that the collisions are strictly binary. Above σ is the differential cross section and Ω is the solid angle. Also the following notation is used: $f = f(\mathbf{r}, \boldsymbol{\xi}; t)$, $f' = f(\mathbf{r}, \boldsymbol{\xi}'; t)$, $f_* = f(\mathbf{r}, \boldsymbol{\xi}_*, t)$, and $f'_* = f(\mathbf{r}, \boldsymbol{\xi}'_*; t)$. Here the primed velocities refer to particles after collision whereas the non-primed ones refer to those before collision. Notice also that as from now on we shall only consider single-particle distribution functions, we have simplified the notation such that we denote these functions simply by f instead of $f^{(1)}$.

2.4 Boltzmann's H-theorem

Let us consider a system where there is no external force. In this case, after sufficiently long time, the system should reach an equilibrium state. By an equilibrium state we understand a state which can be described by such a distribution function which is a solution of the Boltzmann equation and independent of time. As there is no external force, we can also assume that this distribution function is independent of $\mathbf{r}$ [7]. The equilibrium distribution function $f^{eq}(\boldsymbol{\xi})$ is thus a solution of the following equation:

$$\int \mathrm{d}^3\xi_* \int \mathrm{d}\Omega\, \sigma(\Omega)\, |\boldsymbol{\xi} - \boldsymbol{\xi}_*|\, [f^{eq}(\boldsymbol{\xi}'_*) f^{eq}(\boldsymbol{\xi}') - f^{eq}(\boldsymbol{\xi}_*) f^{eq}(\boldsymbol{\xi})] = 0. \tag{2.24}$$

A sufficient condition for a solution of this equation is

$$f^{eq}(\boldsymbol{\xi}'_*) f^{eq}(\boldsymbol{\xi}') - f^{eq}(\boldsymbol{\xi}_*) f^{eq}(\boldsymbol{\xi}) = 0. \tag{2.25}$$

Let us now prove the H-theorem following the procedure of Ref. [8]. We define the H-function as

$$H(t) = \int \mathrm{d}\boldsymbol{\xi} f(\boldsymbol{\xi}, t) \ln f(\boldsymbol{\xi}, t). \tag{2.26}$$

Differentiation of this H-function gives

$$\frac{\mathrm{d}H}{\mathrm{d}t} = \int \mathrm{d}\boldsymbol{\xi}(1 + \ln f(\boldsymbol{\xi}, t))\frac{\partial f(\boldsymbol{\xi}, t)}{\partial t}. \tag{2.27}$$

From Eqs. (2.22) and (2.23) we find that

$$\frac{\partial f}{\partial t} = \int \mathrm{d}\boldsymbol{\xi}_* \int \mathrm{d}\Omega\, \sigma(\Omega)|\boldsymbol{\xi} - \boldsymbol{\xi}_*|[f'_* f' - f_* f] - \boldsymbol{\xi} \cdot \nabla f, \tag{2.28}$$

which can be substituted to Eq. (2.27):

$$\frac{\mathrm{d}H}{\mathrm{d}t} = -\int \mathrm{d}\boldsymbol{\xi}(\boldsymbol{\xi} \cdot \nabla f)(1 + \ln f) + \int \mathrm{d}\,\boldsymbol{\xi} \int \mathrm{d}\boldsymbol{\xi}_* \int \mathrm{d}\Omega\, \sigma(\Omega)|\boldsymbol{\xi} - \boldsymbol{\xi}_*|[f'_* f' - f_* f][1 + \ln f]. \tag{2.29}$$

By applying the Gauss law one can show that first term on the right-hand side vanishes, assuming that $f \to 0$ for large $\mathbf{r}$ and $\boldsymbol{\xi}$. Therefore

$$\frac{\mathrm{d}H}{\mathrm{d}t} = \int \mathrm{d}\,\boldsymbol{\xi} \int \mathrm{d}\boldsymbol{\xi}_* \int \mathrm{d}\Omega\, \sigma(\Omega)|\boldsymbol{\xi} - \boldsymbol{\xi}_*|[f'_* f' - f_* f][1 + \ln f]. \tag{2.30}$$

Change of variables $\boldsymbol{\xi}$ and $\boldsymbol{\xi}_*$ results in

$$\frac{\mathrm{d}H}{\mathrm{d}t} = \int \mathrm{d}\,\boldsymbol{\xi} \int \mathrm{d}\boldsymbol{\xi}_* \int \mathrm{d}\Omega\, \sigma(\Omega)|\boldsymbol{\xi} - \boldsymbol{\xi}_*|[f'_* f' - f_* f][1 + \ln f_*]. \tag{2.31}$$

Summing these two equations gives

$$\frac{\mathrm{d}H}{\mathrm{d}t} = \frac{1}{2}\int \mathrm{d}\,\boldsymbol{\xi} \int \mathrm{d}\boldsymbol{\xi}_* \int \mathrm{d}\Omega\, \sigma(\Omega)|\boldsymbol{\xi} - \boldsymbol{\xi}_*|[f'_* f' - f_* f][2 + \ln f f_*]. \tag{2.32}$$

On the other hand, if we consider the reverse collision, we get

$$\frac{\mathrm{d}H}{\mathrm{d}t} = \frac{1}{2}\int \mathrm{d}\,\boldsymbol{\xi}' \int \mathrm{d}\boldsymbol{\xi}'_* \int \mathrm{d}\Omega\, \sigma(\Omega)|\boldsymbol{\xi}' - \boldsymbol{\xi}'_*|[f'_* f' - f_* f][-2 - \ln f' f'_*]. \tag{2.33}$$

Summing up Eqs. (2.32) and (2.33) we find finally that

$$\frac{\mathrm{d}H}{\mathrm{d}t} = \frac{1}{4}\int \mathrm{d}\,\boldsymbol{\xi} \int \mathrm{d}\boldsymbol{\xi}_* \int \mathrm{d}\Omega\, \sigma(\Omega)|\boldsymbol{\xi} - \boldsymbol{\xi}_*|[f'_* f' - f_* f] \ln \frac{f f_*}{f' f'_*}, \tag{2.34}$$

since $\mathrm{d}\boldsymbol{\xi}\mathrm{d}\boldsymbol{\xi}_* = \mathrm{d}\,\boldsymbol{\xi}'\mathrm{d}\boldsymbol{\xi}'_*$ and $|\boldsymbol{\xi} - \boldsymbol{\xi}_*| = |\boldsymbol{\xi}' - \boldsymbol{\xi}'_*|$ (momentum and energy are conserved in collisions). It is evident that the integrand in Eq. (2.34) is never positive. Thus H-function never increases. This result is known as Boltzmann's H-theorem. On the other hand, we see that when $\mathrm{d}H/\mathrm{d}t = 0$, Eq. (2.25) holds, i.e. the distribution function has reached its equilibrium.

2.5 Maxwell-Boltzmann distribution

Next we calculate the exact form of the equilibrium distribution function, which we have seen to be a solution of Eq. (2.25). Taking a logarithm of this equation gives

$$\ln f^{eq}(\boldsymbol{\xi}'_*) + \ln f^{eq}(\boldsymbol{\xi}') = \ln f^{eq}(\boldsymbol{\xi}_*) + \ln f^{eq}(\boldsymbol{\xi}), \tag{2.35}$$

which has a form of a conservation law. The most general solution to this equation is a sum of all independently conserved quantities. In the case under consideration, these conserved quantities are momentum and energy. Thus the solution must be of the form

$$\log f^{eq}(\boldsymbol{\xi}) = -A\xi^2 + 2A\boldsymbol{\xi}_0 \cdot \boldsymbol{\xi} + (A\xi_0^2 + \log C) \tag{2.36}$$

$$f^{eq}(\boldsymbol{\xi}) = C \exp\left[-A(\boldsymbol{\xi} - \boldsymbol{\xi}_0)^2\right]. \tag{2.37}$$

In Eq. (2.36), the first term on the right-hand side is associated with the energy, the second term with the three components of the momentum, and the last term is an arbitrary constant. Our task is now to determine the five unknown constants A, C, $\boldsymbol{\xi}_0 = (\xi_{0x}, \xi_{0y}, \xi_{0z})$. To this end we use Eqs. (2.19) - (2.21), and obtain the final form of the equilibrium distribution function,

$$f^{eq}(\boldsymbol{\xi}) = \frac{N}{V}\left(\frac{m}{2\pi k_B T}\right)^{3/2} \exp\left[-\frac{m(\boldsymbol{\xi} - \boldsymbol{\xi}_0)^2}{2k_B T}\right]. \tag{2.38}$$

This distribution is the Maxwell-Boltzmann equilibrium distribution function.

2.6 Bhatnagar-Gross-Krook collision function

The collision function derived above may cause difficulties in practical problems because of its complicated form. Bhatnagar, Gross, and Krook (BGK) introduced a phenomenological collision function which has a drastically simplified form, but captures still the essential physics of the kinetic problem [9]. In the BGK approximation, which is also known as the single-relaxation-time approximation, the collision term is replaced by a relaxation term. This approximate collision term describes relaxation of the distribution functions towards the local equilibria which are functions of the local conserved quantities. The BGK collision term has the form

$$\left(\frac{\partial f}{\partial t}\right)_{\text{coll}} = \frac{f^{eq} - f}{\tau}, \tag{2.39}$$

where τ is a relaxation time which represents the time scale related to the relaxation process due to collisions, and f^{eq} is the local equilibrium. The main approximation

in the BGK approximation is the assumption that all modes in the system relax at the same speed described by the relaxation time, and that this process can be described by a constant relaxation time through the whole system. In spite of its drastically simplified form, the BGK collision term gives in many cases a qualitatively correct behaviour.

3 The lattice-Boltzmann equation method

3.1 Overview

In the previous Chapter we saw that the continuity and Navier–Stokes equations result from two basic conservation laws, namely conservation of mass and momentum, together with the constitutive relation Eq. (2.7). Actually, conservation laws at a macroscopic level are reflections of the same principles at the microscopic level. Although flow simulations using molecular dynamics are in most cases inpractical or even impossible, it fortunately turns out that microscopic details of molecular interactions are unimportant, if one is only interested in the behaviour of the fluid at the hydrodynamic level. Therefore, it is possible to construct such artificial microscopic or mesoscopic systems that the essential conservation laws and symmetry requirements are fulfilled, and the correct hydrodynamic behaviour is thus obtained. These systems can be simplified in such a way that microscopic details that are not needed for the hydrodynamics are ignored [10]. This kind of systems can be and have been used in simulations of fluid flow

Examples of this kind of approach include, e.g., lattice-gas cellular automata [2], dissipative particle dynamics [3], and smoothed particle dynamics [4]. Here we briefly review the lattice-gas cellular automata which are predecessors of the lattice-Boltzmann method. In lattice-gas cellular automata, fluid is modelled by fictitious mesoscopic particles moving on a regular lattice. Also time is discretised and particles are only allowed to have a set of discrete velocities such that particles move from one lattice point to another during one time step. The first lattice-gas automaton aimed at simulating fluid flow was introduced in 1973 by Hardy, Pomeau, and de Pazzis (HPP) [11]. The HPP model uses a two-dimensional square lattice which has insufficient symmetries to produce the Navier–Stokes equation. In particular, the HPP model is neither Galilean invariant nor isotropic. In 1986, Frisch, Hasslacher, and Pomeau (FHP) [2] and Wolfram [12] introduced a two-dimensional lattice-gas cellular automaton on a triangular lattice, that was able to simulate the Navier–Stokes equation. This model was immediately generalised to three dimensions [13]. Evolution of the FHP automaton is given by the equation

$$n_i(\mathbf{r} + \mathbf{e}_i, t + 1) - n_i(\mathbf{r}, t) = \Omega_i(n), \tag{3.1}$$

where $i = 1, 2, \ldots, 6$ refer to the six possible (2D) lattice directions in the triangular lattice, n_i and $\mathbf{e}_i$ are the corresponding Boolean particle number and velocity, respectively, and Ω_i is the collision operator which is constructed in such a way that both mass and momentum are conserved in the collisions. Position vector $\mathbf{r}$ points always to a lattice point in the triangular lattice. Notice that the above equation is written in lattice units. The evolution of the FHP fluid is divided into two steps, after the collision process described by the collision operator, particles are moved to neighbouring lattice nodes according to their velocities. Evolution of the system results from iteration of these collision and streaming processes. Lattice-gas automata have some drawbacks: they are noisy and require thus spatial and/or temporal averaging, they are not Galilean invariant, pressure has an unphysical dependence on macroscopic velocity, and there are some unphysical conserved quantities.

The problems that the FHP automaton was facing were cured by taking an ensemble average over Eq. (3.1) [14, 15]. The model thus evolved is known as the lattice-Boltzmann method [17, 18]. In the lattice-Boltzmann method Boolean particle numbers are replaced by the probability of finding a particle at certain lattice point at certain time with certain velocity. In the first lattice-Boltzmann methods the collision operator of the lattice-gas method was replaced by an operator in which the Boolean operations were replaced by corresponding arithmetic operations. With this collision operator lattice-Boltzmann models are however inefficient. Their computational efficiency was improved by linearising the collision operator around the equilibrium distribution [16]. The most used model was obtained by introducing the single-relaxation-time Bhatnagar–Gross–Krook (BGK) approximation [9] for the collision operator [19–22]. Recently different multiple-relaxation-time collision operators [23–28] have attracted a lot of interest since they can improve the numerical stability of the method.

3.2 From the Boltzmann equation to the lattice-Boltzmann equation

In this Section we discretise the Boltzmann equation [29]. Until now we have described our system in terms of the number-distribution function. From now on, in order to follow the usual notation in the lattice-Boltzmann literature, we shall use the mass-distribution function which is obtained by multiplying the number-distribution function by the molecular mass m.

We start from the discrete-velocity Boltzmann-BGK equation

$$\partial_t f_i + \boldsymbol{\xi}_i \cdot \nabla f_i = -\frac{1}{\tau} \left(f_i - f_i^{eq} \right), \tag{3.2}$$

where the velocity space is discretised in such a way that only certain discrete velocities ξ_i are allowed for the particles, and $f_i = f_i(\mathbf{r}, t)$ are the corresponding velocity distribution functions. The macroscopic flow variables are obtained from

$$\rho = \sum_i f_i, \tag{3.3}$$

$$\rho \mathbf{u} = \sum_i \boldsymbol{\xi}_i f_i. \tag{3.4}$$

Equation (3.2) is now made dimensionless by using dimensionless quantities $\hat{\mathbf{e}}_i = \boldsymbol{\xi}/\xi_r$, $\hat{\nabla} = L\nabla$, $\hat{t} = t\xi_r/L$, $\hat{\tau} = \tau/t_c$, and $\hat{f}_i = f_i/\rho_r$. Here caret is used to denote a dimensionless quantity, ξ_r is a reference speed , L a characteristic length scale, t_c the time between successive collisions, and ρ_r a reference density. The reference speed is chosen to be equal to the minimum non-zero velocity, and the reference density is usually chosen such that the average density in the system equals one. In addition to t_c, another time scale is given by the characteristic flow time L/ξ_r. Using these definitions for the dimensionless quantities, we obtain a dimensionless discrete-velocity Boltzmann equation

$$\partial_{\hat{t}} \hat{f}_i + \hat{\mathbf{e}}_i \cdot \hat{\nabla} \hat{f}_i = -\frac{1}{\epsilon \hat{\tau}} \left(\hat{f}_i - \hat{f}_i^{eq} \right), \tag{3.5}$$

where the Knudsen number

$$\epsilon = \frac{t_c \xi_r}{L} \tag{3.6}$$

is the ratio of the collision time to the flow time, or of the mean free path to the characteristic length scale. To keep the notation simple, the carets are not explicitly shown hereafter, although all quantities are assumed to be dimensionless.

We have now discretised the velocity space and written the discrete-velocity Boltzmann equation thus obtained in dimensionless form. Next we shall discretise the space and time in order to obtain a fully discrete equation. To this end, the time derivate is replaced by a first-order finite-difference approximation

$$\partial_t f_i \approx \frac{f_i(\mathbf{r}, t + \delta t) - f_i(\mathbf{r}, t)}{\delta t}, \tag{3.7}$$

and for the convective term we use a first-order upwind space discretisation,

$$\mathbf{e}_i \cdot \nabla f_i \approx \frac{f_i(\mathbf{r} + \mathbf{e}_i \delta t, t + \delta t) - f_i(\mathbf{r}, t)}{\delta r}. \tag{3.8}$$

We choose the lattice spacing δr and time step δt such that $\delta r/\delta t$ is equal to the minimum of the speeds $|\mathbf{e}_i|$, which, with our choice for the reference speed ξ_r, is equal to unity. Finally, by selecting the dimensional time step to be equal to t_c, we obtain the lattice-Boltzmann equation in its standard form:

$$f_i(\mathbf{r} + \mathbf{e}_i \delta t, t + \delta t) = f_i(\mathbf{r}, t) - \frac{1}{\tau} \left(f_i(\mathbf{r}, t) - f_i^{eq}(\mathbf{r}, t) \right). \tag{3.9}$$

Although we used here first-order discretisations, the method obtained has a second-order accuracy both in space and time since the discretisation error has a specific form, and can be included in the viscosity [29]. The set of discrete velocities should be selected such that they comply with the discretisation of space and time, i.e., if $\mathbf{r}$ is a lattice node also $\mathbf{r} + \mathbf{e}_i \delta t$ should be a lattice node for all $\mathbf{e}_i$.

Although the lattice-Boltzmann equation originated historically from the lattice-gas method, it can also be understood as a specific finite-difference discretisation of the continuous Boltzmann equation. The discretisations used are rather primitive, and more sophisticated techniques might lead to methods with enhanced efficiency and stability and more flexible lattice structures. However, the standard lattice-Boltzmann equation has certain appealing properties. Most importantly, we can preserve the interpretation of particles streaming and colliding on a lattice as a heritage from the lattice gases, which is convenient, e.g., when handling boundaries and in the parallelisation of the method. Higher order discretisations would make this kind of interpretation at least more difficult if not impossible.

Several possibilities remain for choosing the lattice structure. In all simulations presented in this Thesis, the three-dimensional 19-velocity (D3Q19) model was used [21]. In this model space is discretised using a cubic lattice and the magnitudes of the possible velocities are 0, 1, and $\sqrt{2}$ corresponding to rest particles and particles moving to nearest or next-nearest lattice nodes. The lattice and the discrete velocities of the D3Q19 model are illustrated in Fig. 3.1. The D3Q19 model is a common choice in the simulations as the models with larger number of velocities, e.g. D3Q27, require more memory, and the models with smaller number of velocities, such as D3Q15 or D3Q13, have some spurious invariants (see, e.g., Ref. [30]).

3.3 Equilibrium distribution function in the D3Q19 model

The last phase in the discretisation procedure is to find a discrete form for the equilibrium distribution function. It has been shown that, for some lattices, both the lattice-Boltzmann equation and the equilibrium distribution function can be obtained by discretising the Boltzmann equation using Gaussian-type quadratures [31]. In this approach the coefficients in the equilibrium distribution function (cf. Eq. (3.12) below) are obtained from the weights of the quadratures. Recently, this type of *a priori* derivation and quadratures needed were presented for the D3Q19 model [32]. However, we derive the equilibrium distribution function in an *a posteriori* fashion by using a low-Mach-number expansion of the Maxwell-Boltzmann

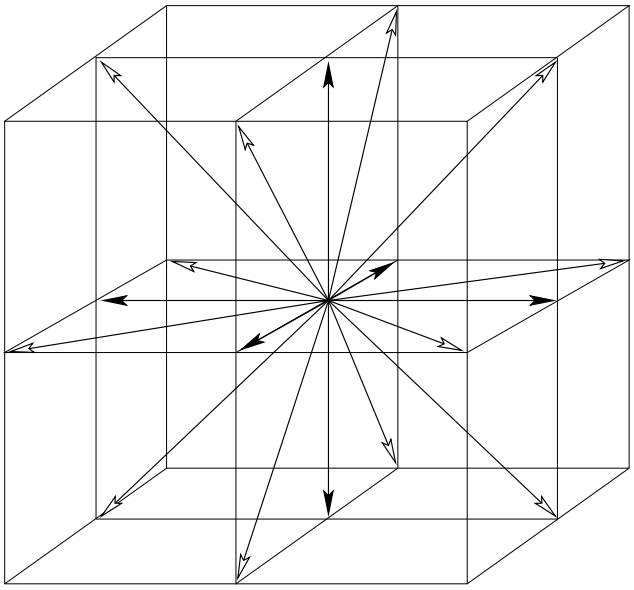

Figure 3.1: Schematic figure of the D3Q19 lattice. Shown are the non-zero lattice vectors. Vectors with filled arrowhead correspond to lattice directions with velocity 1 and the other to those with velocity$\sqrt{2}$. In addition, the D3Q19 model has rest particles with zero velocity.

distribution function with some unknown weight coefficients for different directions, and determining these weights by requiring the equilibrium distribution to fulfil appropriate isotropy conditions.

The starting point is a second-order Taylor polynomial of the Maxwell-Boltzmann distribution function,

$$f^{eq}(\xi) = \rho\left(\frac{m}{2\pi k_B T}\right)^{3/2} \exp\left[-\frac{m(\xi-\mathbf{u})^2}{2k_B T}\right] \tag{3.10}$$

$$\approx \rho\left(\frac{m}{2\pi k_B T}\right)^{3/2} \exp\left[-\frac{m\xi^2}{2k_B T}\right] \times \left[1+\left(\frac{m}{k_B T}\right)\boldsymbol{\xi}\cdot\mathbf{u}+\frac{1}{2}\left(\frac{m}{k_B T}\right)^2(\boldsymbol{\xi}\cdot\mathbf{u})^2-\frac{1}{2}\left(\frac{m}{k_B T}\right)u^2\right]. \tag{3.11}$$

Based on this expression we choose the following form for the discretised equilibrium distribution function:

$$f_i^{eq} = \rho t_i\left(1+\frac{e_{i\alpha}u_\alpha}{c_s^2}+\frac{e_{i\alpha}e_{i\beta}u_\alpha u_\beta}{2c_s^4}-\frac{u^2}{2c_s^2}\right), \tag{3.12}$$

where we have the speed of sound of the lattice-Boltzmann fluid $c_s = (k_B T/m)^{1/2}$. The weight factor t_i may have three different value, w_0 for the rest particles, and

w_1 and $w_{\sqrt{2}}$ for particles moving to nearest-neighbour and next-nearest-neighbour lattice nodes, respectively. The values of constants w_0, w_1, $w_{\sqrt{2}}$ and c_s must be determined in such a way that no numerical artefacts arise in the hydrodynamic behaviour of the model due to discretisation.

To ensure the isotropy we require that the velocity moments of the discretised zero-velocity equilibrium distribution function ($f_i^{eq}(\mathbf{u}=0)$) equal those of the continuous case up to fourth order, since these moments influence the incompressible hydrodynamics [19]. By evaluating these moments for the continuous case we obtain the following conditions:

$$\sum_i t_i = 1, \tag{3.13}$$

$$\sum_i t_i e_{i\alpha} e_{i\beta} = c_s^2 \delta_{\alpha\beta}, \tag{3.14}$$

$$\sum_i t_i e_{i\alpha} e_{i\beta} e_{i\gamma} e_{i\mu} = c_s^4 \left(\delta_{\alpha\beta}\delta_{\gamma\mu} + \delta_{\alpha\gamma}\delta_{\beta\mu} + \delta_{\alpha\mu}\delta_{\beta\gamma}\right). \tag{3.15}$$

In addition, we notice that the odd-rank lattice tensors vanish. The last one of the above equations gives two independent conditions, one corresponding to the case $\alpha = \beta = \gamma = \mu$ and another to $\alpha = \beta \neq \gamma = \mu$. Thus we have four equations for the four unknowns. Solving these equations we find $w_0 = 1/3$, $w_1 = 1/18$, $w_{\sqrt{2}} = 1/36$, and $c_s^2 = 1/3$.

3.4 Chapman–Enskog analysis

In this Section we show that the pressure and velocity fields produced by the lattice-Boltzmann model obey the Navier–Stokes equation, i.e. the lattice-Boltzmann method is suitable for fluid-flow simulations. We use the D3Q19 model with the BGK collision operator together with the equilibrium distribution function derived above. For simplicity and without loss of generality, we use here lattice units in which the time step and lattice spacing equal one.

We start by taking a perturbative expansion for the distribution function,

$$f_i = f_i^{(0)} + \epsilon f_i^{(1)} + \epsilon^2 f_i^{(2)} + \cdots. \tag{3.16}$$

Here the small perturbation ϵ is the Knudsen number. The space and time derivatives are also expressed in terms of multiscale variables,

$$\partial_\alpha = \epsilon \partial_{1\alpha}, \tag{3.17}$$

$$\partial_t = \epsilon \partial_{t_1} + \epsilon^2 \partial_{t_2} + \cdots. \tag{3.18}$$

The physical background of this multiscale formalism is that different physical phenomena such as inertial propagation and dissipation occur at different time scales [33]. We use the so-called Chapman–Enskog assumption and require that

$$f_i^{(0)} = f_i^{eq}, \tag{3.19}$$

$$\rho = \sum_i f_i = \sum_i f_i^{(0)}, \tag{3.20}$$

$$\rho \mathbf{u} = \sum_i \mathbf{e}_i f_i = \sum_i \mathbf{e}_i f_i^{(0)}. \tag{3.21}$$

These requirements imply that

$$\sum_i f_i^{(k)} = 0, \tag{3.22}$$

$$\sum_i \mathbf{e}_i f_i^{(k)} = 0, \tag{3.23}$$

for $k \geq 1$.

Taylor expansion of the lattice-Boltzmann equation (Eq. (3.9)) is

$$(\partial_t + e_{i\alpha}\partial_\alpha) f_i + \frac{1}{2}(\partial_t + e_{i\alpha}\partial_\alpha) f_i + \cdots = -\frac{1}{\tau}(f_i - f_i^{eq}), \tag{3.24}$$

which, by using expansions of Eqs. (3.16) - (3.18), can be written as

$$\begin{aligned} &\left(\epsilon\partial_{t_1} + \epsilon^2\partial_{t_2} + \epsilon e_{i\alpha}\partial_{1\alpha}\right)\left(f_i^{(0)} + \epsilon f_i^{(1)} + \epsilon^2 f_i^{(2)}\right) + \\ &\frac{1}{2}\left(\epsilon\partial_{t_1} + \epsilon^2\partial_{t_2} + \epsilon e_{i\alpha}\partial_{1\alpha}\right)\left(\epsilon\partial_{t_1} + \epsilon^2\partial_{t_2} + \epsilon e_{i\beta}\partial_{1\beta}\right)\left(f_i^{(0)} + \epsilon f_i^{(1)} + \epsilon^2 f_i^{(2)}\right) \\ &= -\frac{1}{2}\left(\epsilon f_i^{(1)} + \epsilon^2 f_i^{(2)}\right). \end{aligned} \tag{3.25}$$

The terms of the order $\mathcal{O}(\epsilon)$ in Eq. (3.25) give

$$\left(\partial_{t_1} + e_{i\alpha}\partial_{1\alpha}\right) f_i^{(0)} = -\frac{1}{\tau} f_i^{(1)}. \tag{3.26}$$

By summing over i and utilising Eqs. (3.19) - (3.23), we obtain the result

$$\partial_{t_1}\rho + \partial_{1\alpha}\left(\rho u_\alpha\right) = 0. \tag{3.27}$$

Multiplying both sides of the Eq. (3.26) by $e_{i\beta}$, summing over i, we find that

$$\partial_{t_1}\left(\rho u_\beta\right) + \partial_{1\alpha}\Pi_{\alpha\beta}^{(0)} = 0, \tag{3.28}$$

where the momentum-flux tensor of zeroth order is defined as

$$\Pi_{\alpha\beta}^{(0)} = \sum_i e_{i\alpha} e_{i\beta} f_i^{(0)}. \tag{3.29}$$

The terms of order $\mathcal{O}(\epsilon^2)$ in Eq. (3.25) form an equation

$$\left[\partial_{t_2} + \frac{1}{2}\left(\partial_{t_1} + e_{i\alpha}\partial_{1\alpha}\right)\left(\partial_{t_1} + e_{i\beta}\partial_{1\beta}\right)\right] f_i^{(0)} + \left(\partial_{t_1} + e_{i\alpha}\partial_{1\alpha}\right) f_i^{(1)} = -\frac{1}{\tau} f_i^{(2)}. \tag{3.30}$$

After summing over i we find that

$$\partial_{t_2}\rho = 0. \tag{3.31}$$

Multiplying both sides of Eq. (3.30) by $e_{i\beta}$ and summing over i gives

$$\partial_{t_2}\left(\rho u_\beta\right) + \partial_{1\alpha}\Pi_{\alpha\beta}^{(1)} = 0, \tag{3.32}$$

where the first-order momentum-flux tensor is given by

$$\Pi_{\alpha\beta}^{(1)} = \left(1 - \frac{1}{2\tau}\right)\sum_i e_{i\alpha} e_{i\beta} f_i^{(1)}. \tag{3.33}$$

Combination of the first and second order results given by Eqs. (3.27) and (3.31) gives the continuity equation

$$\partial_t \rho + \partial_\alpha\left(\rho u_\alpha\right) = 0. \tag{3.34}$$

Similarly by combining the first order result of Eq. (3.28) and the second order result of Eq. (3.32), we arrive at the momentum equation

$$\partial_t\left(\rho u_\beta\right) + \partial_\alpha \Pi_{\alpha\beta} = 0, \tag{3.35}$$

where the momentum-flux tensor is

$$\Pi_{\alpha\beta} = \Pi_{\alpha\beta}^{(0)} + \epsilon\Pi_{\alpha\beta}^{(1)}. \tag{3.36}$$

Next we show that the momentum-flux tensor defined above is valid and reproduces the Navier–Stokes equation for incompressible flows. To this end we need to calculate the explicit expression for the momentum-flux tensor, which is done by using the the equilibrium distribution function given by Eq. (3.12). For the zeroth-order momentum-flux tensor we obtain the expression

$$\Pi_{\alpha\beta}^{(0)} = c_s^2\rho\delta_{\alpha\beta} + \rho u_\alpha u_\beta = p\delta_{\alpha\beta} + \rho u_\alpha u_\beta. \tag{3.37}$$

From this equation, we find that the pressure in this model obeys the ideal gas law,

$$p = c_s^2\rho. \tag{3.38}$$

The first-order momentum-flux tensor can be calculated by substituting Eq. (3.26) into Eq. (3.33). In the incompressible limit, i.e when $\partial_t\rho = 0$ and $\partial_\alpha u_\alpha = 0$, we obtain

$$\epsilon\Pi_{\alpha\beta}^{(1)} = -\nu\rho\left(\partial_\alpha u_\beta + \partial_\beta u_\alpha\right), \tag{3.39}$$

where the terms of order $\mathcal{O}(u^3)$ have been ignored, and the kinematic viscosity is given by

$$\nu = \frac{2\tau - 1}{2} c_s^2 = \frac{2\tau - 1}{6}. \tag{3.40}$$

Now, with the help of these results, the momentum equation (Eq. (3.35)) can be written as

$$\partial_t u_\beta + u_\alpha \partial_\alpha u_\beta = -\frac{1}{\rho} \partial_\beta p + \nu \partial_\alpha^2 u_\beta, \tag{3.41}$$

which is the Navier–Stokes equation for incompressible flow. Since the lattice-Boltzmann fluid obeys the equation of state of the ideal gas, the fluid is actually compressible, and simulations should be done in the low-Mach-number ($Ma = u/c_s$) limit. In addition reference frame should be chosen such that flow speed is small in order to keep the momentum fluxes due to the terms of order $\mathcal{O}(u^3)$ negligible [34, 35]. In practice one should not exceed the velocity 0.1 (in lattice units).

The analysis above gives a useful result: in lattice-Boltzmann simulations the deviatoric stress tensor can be calculated locally from the distribution values using the approximation $f_i^{(1)} \approx f_i^{neq} = f_i - f_i^{eq}$ where f_i^{neq} is the non-equilibrium part of the distribution function (cf. Eq. (3.33)),

$$\sigma'_{\alpha\beta} = -\left(1 - \frac{1}{2\tau}\right) \sum_i e_{i\alpha} e_{i\beta} \left(f_i - f_i^{eq}\right). \tag{3.42}$$

There is no need for numerical differentiation of the velocity field as is the case in the conventional methods in computational fluid dynamics, and stresses are obtained at low computational cost.

Finally we point out that the lattice-Boltzmann equation can also be used to simulate Stokes flow. For this purpose the equilibrium distribution function has to be modified such that

$$f_i^{eq} = t_i \left(1 + \frac{e_{i\alpha} u_\alpha}{c_s^2}\right). \tag{3.43}$$

The zeroth-order momentum-flux tensor obtained from this linear form of the equilibrium distribution function is

$$\Pi_{\alpha\beta}^{(0)} = p\delta_{\alpha\beta}, \tag{3.44}$$

which differs from the previously obtained form so that it has no convective term. Thus simulations with this equilibrium distribution function produce flows that obey the Stokes equation.

3.5 Shan–Chen multiphase model

The lattice-Boltzmann method in its standard form has an equation of state of the ideal gas. If we want to simulate systems with multiple phases, an additional multiphase model is needed. Several multiphase models for the lattice-Boltzmann method exist. The most widely used models are the colour-gradient model [36], the Shan–Chen model (model of local interactions) [37], and the free-energy model [38]. These models have been criticised, since they have some inconsistencies (see e.g. Ref. [39]). Some new models have been proposed recently [40, 41], which should have a more solid physical origin. Unfortunately, no reported numerical simulations exist where these models would have been used. In Ref. [42], a modification of the model presented in Ref. [41] was used to simulate some physical phenomena. According to Lee and Lin [43], this modified model has some new inconsistensies, however.

Here we give a brief review of the Shan–Chen model which is used in the simulations described in next Chapter. The Shan–Chen model has successfully been used in simulating flows in porous media [44–46]. As we are interested in large systems, an attractive property of the Shan–Chen model is that it needs only one set of distribution functions f_i when simulating liquid-vapour flows. In other alternatives two sets of distribution functions are needed, and thus also a double amount of memory.

In the Shan–Chen model interactions are added between neighbouring fluid nodes. This cohesive force leads to phase separation in the system so that the fluid has two equilibrium densities, i.e. a vapour phase and a liquid phase. The cohesive interaction is incorporated by adding to each fluid node an extra force

$$F_G(\mathbf{r},t) = -\psi(\mathbf{r},t)\sum_i G_i\psi(\mathbf{r}+\mathbf{e}_i,t)\mathbf{e}_i, \tag{3.45}$$

where the effective mass $\psi(\mathbf{r},t) = 1-\exp(-\rho)$, and

$$G_i = \begin{cases} 2G & \text{for } |\mathbf{e}_i| = 1 \\ G & \text{for } |\mathbf{e}_i| = \sqrt{2} \\ 0 & \text{for } |\mathbf{e}_i| = 0 \end{cases} \tag{3.46}$$

for the D3Q19 model. Notice that $G_i = 36Gt_i$ ensuring the isotropy of the model. Models with higher degree of isotropy were recently introduced [47] so as to reduce the spurious currents arising at the liquid-vapour interface. These models, however, require interactions of longer range. The parameter G is used to control the strength of the cohesive force and thus the magnitude of surface tension. The effective mass ψ is chosen such that when ρ is small $\psi \propto \rho$, and when ρ is large

ψ approaches a constant value. It has been shown that this choice leads to a thermodynamic inconsistency of the method [39, 48]. The only choice leading to no inconsistencies would be $\psi \propto \rho$. This choice is however out of question since it ignores the effect of repulsive core, i.e. it leads to mass collapse where density tends to infinity. Therefore, we have chosen the effective mass similarly to the original article of Shan and Chen [37].

A similar approach can be used to simulate wetting phenomena. To model the interaction between fluid and solid, Martys and Chen introduced another additional interaction [44]. This force has a similar form as the cohesive force, and can be written as

$$F_W = -\psi(\mathbf{r}, t) \sum_i W_i s(\mathbf{r} + \mathbf{e}_i, t)\mathbf{e}_i, \tag{3.47}$$

where $s = 0, 1$ for the fluid and solid nodes, respectively, and

$$W_i = \begin{cases} 2W & \text{for } |\mathbf{e}_i| = 1 \\ W & \text{for } |\mathbf{e}_i| = \sqrt{2} \\ 0 & \text{for } |\mathbf{e}_i| = 0 \end{cases} . \tag{3.48}$$

The strength of this adhesive force is controlled by parameter W. It is sometimes erroneously claimed that a negative value of W leads to a wetting liquid and a positive value to a non-wetting liquid. This is however not true in the case of a multiphase fluid. Reason for this is that also the cohesive force contributes to the fluid-solid interaction. The actual transition from a wetting to a non-wetting liquid happens when W is clearly negative, actual value depending on the parameter G (see Ref. [II]).

One consequence of this interplay between the forces at walls is that the density of the fluid in liquid phase is lower near the walls than in the bulk. This feature leads on the other hand to a slip velocity at the walls even when the no-slip boundary condition is imposed [46]. However, some authors have used this property when studying slip in hydrophobic microchannels [49, 50]. One possibility to avoid an unwanted slip velocity in the multiphase fluid system could be to set the component perpendicular to the wall of the cohesive force equal to zero for the nodes next to the wall, as was done by Kang *et al.* [51] in the case of the Shan–Chen multicomponent model. This can indeed be done when performing simulations in simple geometries such as flow between parallel plates, as was the case in Ref. [51], or more generally, when the exact position and the surface normal of the wall are known. As we are interested in multiphase flows in more complex geometries, we are not able to follow their suggestion, however.

The effect of both the cohesive and the adhesive forces are added into the lattice-Boltzmann formalism in the relaxation process, using a modified velocity deter-

mined from the equation

$$\rho \mathbf{u}' = \rho \mathbf{u} + \tau(\mathbf{F}_G + \mathbf{F}_W) \tag{3.49}$$

in the equilibrium distribution function.

The addition of cohesive force leads to a modified equation of state. The force term can be expanded, in the first order [52], such that

$$\begin{aligned} \mathbf{F}_G &\approx -36\psi G \sum_i t_i \left(\psi + \mathbf{e}_i \cdot \nabla\psi\right) \mathbf{e}_i & (3.50) \\ &= -\nabla\left(18 G c_s^2 \psi^2\right). & (3.51) \end{aligned}$$

This force modifies the pressure that becomes

$$p = c_s^2 \rho + 18 G c_s^2 \psi^2 = \frac{1}{3}\rho + 6 G \psi^2. \tag{3.52}$$

From the equation above we see that phase separation occurs if G is sufficiently negative and ψ is an increasing but bounded (no mass collapse) function of ρ.

The Shan–Chen model produces also a surface tension at the interface between the liquid and vapour phases. The magnitude of surface tension depends on parameter G, and is obtained from numerical simulations. For example, one can simulate droplets with varying radius and calculate the pressure difference across the liquid-vapour interface. Surface tension is then obtained from the Laplace law which says that the pressure difference equals surface tension multiplied by the inverse radius of the droplet [37, 44, 53].

It is evident that the Shan–Chen model does not conserve momentum locally due to the forces added. However, momentum is conserved globally [37]. This can be seen by calculating the total momentum change in the system. By summing over all lattice nodes, we obtain

$$\Delta \boldsymbol{P} = \sum_{\boldsymbol{r}} \boldsymbol{F}(\boldsymbol{r}) = -\sum_{\boldsymbol{r},i} G_i \psi(\boldsymbol{r}) \psi(\boldsymbol{r} + \boldsymbol{e}_i) \boldsymbol{e}_i. \tag{3.53}$$

Since $\boldsymbol{e}_i$ is a dummy variable we can replace it with $-\boldsymbol{e}_i$. This yields

$$\Delta \boldsymbol{P} = \sum_{\boldsymbol{r},i} G_i \psi(\boldsymbol{r}) \psi(\boldsymbol{r} - \boldsymbol{e}_i) \boldsymbol{e}_i. \tag{3.54}$$

If the boundary conditions are such that there is no momentum flux from the boundaries (this is the case with, e.g., periodic boundary conditions) also $\boldsymbol{r}$ is a dummy variable and we can replace $\boldsymbol{r} - \boldsymbol{e}_i$ with $\boldsymbol{r}$. This gives the net momentum change

$$\Delta \boldsymbol{P} = \sum_{\boldsymbol{r},i} G_i \psi(\boldsymbol{r} + \boldsymbol{e}_i) \psi(\boldsymbol{r}) \boldsymbol{e}_i = -\Delta \boldsymbol{P}. \tag{3.55}$$

Hence we have $\Delta \boldsymbol{P} = 0$, i.e. the momentum is conserved.

3.6 Solid boundaries

A boundary condition is needed when a fluid node is next to a solid node. In that case some of the distribution functions f_i are unknown after the streaming process. The task of the boundary condition is to determine the values of these unknown quantities. The most common boundary condition is the so-called no-slip boundary where the velocity of the fluid close to a wall equals the velocity of wall.

3.6.1 Bounce-back boundary condition

In lattice-Boltzmann simulations solid boundaries are usually introduced into the system by the so-called bounce-back boundary condition. This boundary condition is simple to implement, computationally very efficient, and can be used for arbitrary shaped boundaries. These issues have enabled the simulations in complicated geometries such as flow through porous media. The bounce-back boundary condition has been maybe the most important factor in the success of the lattice-Boltzmann method. On the other hand, bounce back is in some sense also the weakest point in lattice-Boltzmann simulations: bounce back is only first-order accurate [54, 55] (except in some special cases), whereas the lattice-Boltzmann method itself is second-order accurate in the interior fluid nodes. Therefore bounce-back treatment for boundaries degrades the accuracy of such lattice-Boltzmann simulations that include solid walls.

The bounce-back scheme is a heuristic boundary treatment which was inherited from the lattice-gas method [12, 56]. In the bounce-back method the particles (in lattice gas) or distribution functions (in lattice Boltzmann) simply scatter from wall nodes thus fixing the unknown distribution functions the via relation

$$f_i(\mathbf{r}, t+1) = f_{-i}(\mathbf{r}, t), \tag{3.56}$$

where $-i$ refers to the direction opposite to direction i, $\mathbf{e}_{-i} = -\mathbf{e}_i$, and $\mathbf{e}_{-i}$ points to a solid node. One of the advantages of this method is that it conserves the mass. Several improved boundary conditions have been proposed [57–60]. These boundary conditions are second-order accurate for simple geometries with straight walls but are difficult to extent to arbitrary surface geometries. On the other hand it has been shown that, for simple flows confined by straight walls such as Poiseuille or Couette flows, even the bounce-back scheme produces a second-order convergence of the error if the wall is located between the solid and fluid nodes [61]. It has also been pointed out that bounce back works quite well when the BGK relaxation time is $\tau \approx 1.0$, but the slip at the wall grows strongly especially for large

values of τ [59, 60]. However, when multiple-relaxation-time models are used, the slip velocity is better under control (see e.g. Refs. [62, 63]).

Recently, several boundary treatments have been proposed for curved geometries [64–72]. These methods are not automatically second-order convergent, however. For example, the method developed by Verberg and Ladd [68] shows only first-order convergence for a Poiseuille flow in an inclined channel. The Bouzidi method [69] has second-order convergence, but, on the other hand, it does not conserve the mass.

3.6.2 Moving walls and force evaluation

Several applications include moving boundaries, such as suspended particles moving in the fluid or moving walls that are used to achieve a shear flow. Ladd [26] generalised the bounce-back condition for moving boundaries. For this boundary condition the scattered distribution function is given by

$$f_i(\mathbf{r}, t+1) = f_{-i}(\mathbf{r}, t) + \frac{2\rho t_i}{c_s^2}(\mathbf{u_b} \cdot \mathbf{e}_i), \tag{3.57}$$

where $\mathbf{u}_b$ is the velocity of the moving boundary. This equation can be understood as follows [73]: the distribution functions are transformed by a Galilean transformation to a frame of reference where the moving wall is at rest, then a normal bounce-back scheme is used, and finally the distributions are transformed back to the original frame of reference. Notice that the rule of Eq. (3.57) reduces to the ordinary bounce-back rule when $u_b = 0$.

Evaluation of the force acting on solid obstacles is of great importance in several applications where the fluid-structure interaction has a central role, e.g. in suspension flows. There exist two different approaches for calculating the force: the momentum-exchance method [26] and the stress-integration method [74]. In the first method the force is calculated from the momentum transfer due to the bounce-back rule, Eq. (3.57), i.e. the force acting on a boundary at $\mathbf{r}_b$ is

$$\mathbf{F}\left(\mathbf{r}_b, t\right) = \sum_i \left(2f_i(\mathbf{r}_b, t) + \frac{2\rho t_i}{c_s^2}\mathbf{u}_b \cdot \mathbf{e}_i\right)\mathbf{e}_i. \tag{3.58}$$

In this summation we only include such directions i for which the generalised bounce-back rule is used. The total force acting on the obstacle is then obtained by summing over all boundary points,

$$\mathbf{F}_T = \sum_{\mathbf{r}_b} \mathbf{F}\left(\mathbf{r}_b, t\right). \tag{3.59}$$

Similarly, the total torque is calculated by summing the torques due to the forces,

$$\mathbf{T}_T = \sum_{\mathbf{r}_b} (\mathbf{r}_b - \mathbf{R}) \times \mathbf{F}(\mathbf{r}_b, t), \tag{3.60}$$

where $\mathbf{R}$ is the centre of mass of the obstacle. In the stress-integration method the total force acting on a particle is calculated by integrating the stress tensor over the particle surface,

$$\mathbf{F}_T = \int_S \boldsymbol{\sigma} \cdot d\mathbf{S} = \int_S [-p\mathbb{I} + \mu(\nabla\mathbf{u} + (\nabla\mathbf{u})^\intercal)] \cdot \mathrm{d}\mathbf{S}. \tag{3.61}$$

These two approaches have been investigated and compared in a detailed manner by Mei et al [75]. They found that the momentum-exchange method is superior to the stress-integration method, and assumed that this is due to the fact that, in the former method, force is calculated directly from the distribution functions whilst in the latter force is obtained indirectly. Mei and co-workers argued that the momentum-exchange method is a reliable, accurate, and easy to implement. On the other hand, stress integration is computationally laborous and more difficult to implement, especially in the three-dimensional case. Also, fluctuations in the force are larger in the stress-integration method.

3.7 Suspensions with spherical particles

The lattice-Boltzmann method has been rather successful in simulations of the behaviour of particle suspensions. Most of the work has focused on particles having a size of several lattice spacings. In the majority of this kind of simulations the coupling between the fluid and solid phases has been realised by the method described above, see e.g. Refs. [26, 76–87]. However, recently also approaches based on the immersed-boundary methods have been used [88–90]. Some work has been performed with sub-grid-scale particles or by considering suspended particles as a continuum and solving an advection-diffusion equation coupled with the fluid-flow simulator [91–93].

In this work particles larger than one lattice unit were used. This enabled us to solve the flow field between particles and to calculate the internal stresses of individual particles. The price one had to pay of this accurate description of the suspension was that number of particles in the simulated systems was rather small, i.e. simulations of industrial-scale systems could not be done with the computational power available at the moment.

Here we will only consider monodispersed suspension, where particles have a spherical shape with a diameter larger than one lattice unit. The framework for

lattice-Boltzmann simulations of suspensions was developed by Ladd [26]. A peculiar property of the Ladd's original model is that the particles are not actually solid ones but hollow shells with an internal fluid. This model has been successfully applied to simulating suspensions, but it has also some artefacts related to the time that the internal fluid needs for relaxing after changes in particle velocity. Another drawback of the Ladd method is that particles must have a density larger than the fluid density to avoid numerical instabilities.

An alternative scheme for suspension simulations was developed by Aidun and co-workers [77]. In the Aidun model the internal fluid has been removed. This eliminates the above mentioned problems related to the internal fluid. However, new problems emerge. As a particle moves over the lattice, nodes previously located under the particle are uncovered, and a method to create fluid to these nodes is needed. We use the equilibrium distribution function with the velocity of particle boundary in order to create new fluid. At the same time, fluid nodes may be covered by particles, and this fluid needs to be removed. Thus fluid mass in the Aidun model is not strictly conserved. Another problem related to the Aidun model arises in the situation where two particles come in close contact so that there are no fluid nodes left between the surfaces of the particles. This situation leads to an unphysically low pressure between the particles. This problem can be solved by adding 'virtual' fluid in the nodes inside particles next to the particle surface. Here the equilibrium distribution functions with velocity of the particle boundary and the average fluid density are used [IV]. This virtual fluid has no effect unless particles come in close contact.

Also models that slightly differ from these two main approaches have been proposed. In the model developed by Behrend particles are also filled by fluid, but solid-fluid interaction takes place at lattice nodes. In addition a "relaxed bounce-back method at the nodes" is used [78]. This method simplifies the Ladd's algorithm. Another modification to the Ladd method has been proposed by Heemels et al. who developed a method to remove the artefacts of the internal fluid without removing the fluid itself [79]. The model of Heemels et al. is however rather complicated, and it has not been used by other authors.

Which model one should choose to use for simulations is partially a matter of taste, since both the method with and the one without interior fluid have shown their capability to produce realistic results. We have chosen the Aidun method in order to keep the possibility to vary the density of the particles more freely.

The algorithm used in lattice-Boltzmann suspension simulations can be described as follows. The lattice-Boltzmann method is used to solve the flow field in the fluid phase of the suspension. Forces and torques acting on individual particles are calculated as described in Section 3.6.2, i.e. using Eqs. (3.59) and (3.60). The motion

of particles is governed by Newtonian dynamics. Both the translational and the rotational motion is allowed in our simulations. The equations of motion for the particles can be integrated by using methods known from molecular dynamics (cf. Ref. [94]), and new positions and velocities of the particles are thus obtained.

When two particles close to each other have a non-zero relative motion, so-called lubrication forces arise. It has been shown that when the distance between particle surfaces is larger than (approximately) one lattice unit, the lattice-Boltzmann method is capable of solving lubrication forces correctly (see e.g. [26]). However, when particles are coming in close contact, typically when the gap between particles is less than a lattice unit, a more accurate description of the flow between the particles would be needed, and the lattice-Boltzmann method fails to reproduce the correct lubrication interaction. Recently, two schemes for the lubrication-force correction have been developed [95, 96]. We have used the correction proposed by Nguyen and Ladd [95], in which an additional force

$$\mathbf{F}_{lub} = \begin{cases} -6\pi\mu \frac{a_1^2 a_2^2}{(a_1+a_2)^2} \left(\frac{1}{h} - \frac{1}{h_N}\right) \mathbf{U}_{12} \cdot \hat{\mathbf{R}}_{12} \hat{\mathbf{R}}_{12}, & h < h_N \\ 0, & h > h_N \end{cases} \tag{3.62}$$

is added between particle pairs. Here μ is the dynamic viscosity of the fluid, a_1 and a_2 are the radii of the particles, h is the distance between the particle surfaces, $\mathbf{U}_{12} = \mathbf{U}_1 - \mathbf{U}_2$ is the velocity difference between the particles, and $\mathbf{R}_{12}$ is a unit vector pointing from the centre of particle 1 to that of particle 2. The cut-off distance h_N tells the distance below which the correction is needed and can be deduced from simulations. For distances $h > h_N$ the lattice-Boltzmann method is able to produce the hydrodynamic interaction correctly and no correction is needed. This correction accounts only for the normal component of the lubrication correction. The tangential component is much weaker and has thus been ignored in our simulations.

Lubrication correction is necessary especially when a coarse discretisation for the particles is used. Unfortunately, at small interparticle distances the divergent lubrication force may lead to large accelerations and thus to numerical instabilities if an explicit velocity update is used. However, using an implicit velocity update has also problems since it leads to a problem with a computational complexity of $\mathcal{O}(n^3)$, where n is the number of particles. Nguyen and Ladd developed a "cluster implicit method", where an implicit update is only used when necessary, i.e. in groups of particles (or clusters) where distances between particle surfaces are less than h_N [95]. The computational cost of their method depends mainly on the maximum cluster size in the system. The cluster implicit method is, however, not suitable for our purposes since we are mainly interested in dense suspensions with large numbers of particles. In this kind of suspension the maximum cluster size typically becomes large. Also, parallelisation of the cluster implicit method would be laborous.

To this end, we have used a simpler, even if less rigorous, method where we have set a minimum value for the distance h, and thus restricted the lubrication force to values ensuring the numerical stability of our simulations. To prevent particle overlaps we added elastic collisions between such pairs of particles which are coming too close to each others. For the particle pairs that still tend to overlap, also a small repulsive velocity-independent force was used [IV]. With these modifications we found that the simulations were stable and no particle overlaps occurred, at least for sufficiently small shear rates and/or solid volume fractions.

4 Two-phase flow in paper

4.1 Wetting and capillarity

If a liquid droplet is placed in contact with a solid surface it exhibits different wetting behaviour depending on the properties of the liquid, the surface, and the surrounding gas. The wetting behaviour of a liquid is characterised by the contact angle θ that liquid forms with the solid at the three-phase contact line. In a case where contact angle is less than 90° ,liquid is called wetting (cf. Fig. 4.1), and when the contact angle is greater than 90°, liquid is called non-wetting. Sometimes, if one wants to connect wetting behaviour with the surface, one says that surface is hydrophilic or hydrophobic. In spite of this terminology, wetting behaviour is neither a property of the liquid nor the solid phases alone but results from minimisation of the interfacial free energies of the liquid-solid, liquid-vapour, and vapour-solid interfaces, and thus depends on properties of all phases involved. For a liquid droplet on an ideal flat and chemically homogeneous surface, this minimisation gives contact angle [97]

$$\cos\theta = \frac{\gamma_{SV} - \gamma_{SL}}{\gamma_{LV}}, \tag{4.1}$$

where γ_{ij} is the free energy per unit area of phases i and j, and V, L, and S stand for the vapour, liquid, and solid, respectively. Free energy γ_{LV} is known simply as surface tension, and is denoted hereafter simply with γ. The above expression for contact angle is known as the Young's equation. In practice surface heterogeneities have a significant effect on contact angle. These heterogeneities also cause the so-called contact-angle hysteresis, i.e. a macroscopic (apparent) contact angle is not uniquely defined but varies between minimum and maximum values which are called the receding and advancing contact angle, respectively.

Wetting and non-wetting liquids behave in opposite manners when meeting with a capillary tube. A wetting liquid fills the tube and rises inside the tube up to a level higher than that of the liquid outside the tube. On the other hand, a non-wetting liquid escapes the tube and the liquid level inside the tube is below the level outside. In other words, a wetting liquid spontaneously fills capillaries, but an external pressure is needed to force a non-wetting liquid to enter a tube. Similar behaviour is observed also when liquids meet more complex capillary systems such as porous media.

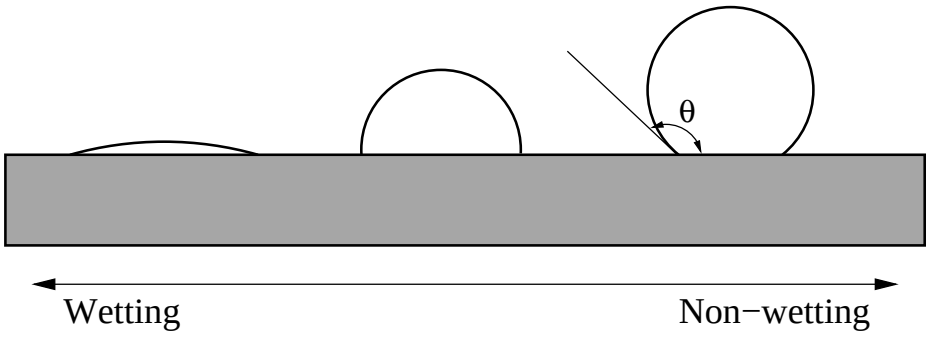

Figure 4.1: Three droplets with dissimilar wettability resting on a solid surface. In the right-hand droplet the contact angle is shown.

In spite of its simplicity, a liquid column in a capillary is an important system in porous-media research, and many models considering the behaviour of liquids in porous materials are based on expressions derived for a single capillary. Therefore, we next consider non-wetting and wetting liquids in single capillaries. In both cases gravity is neglected since in the applications considered later, gravity is not important.

First we consider a static non-wetting case. An external pressure is needed to force the liquid to intrude inside a capillary tube with radius a. Let the pressure needed to keep the liquid column in equilibrium in the tube be Δp. Capillary force tries in this case to expel the liquid from the tube. Balancing the extruding force (capillary force) and the intruding force (external pressure) leads to so-called Washburn equation [98]

$$\Delta p = \frac{2\gamma \cos\theta}{a}. \tag{4.2}$$

The Washburn equation is used, e.g., for interpreting the measurement data in mercury-intrusion porosimetry.

Next we consider capillary penetration of a wetting, viscous, and incompressible liquid in a single capillary tube. Since the liquid is wetting, it spontaneously rises in the tube. Let us consider the case where the flow in tube is laminar and fully developed (Poiseuille flow). By applying Newton's second law on a column of liquid, we obtain

$$\rho\left[z\frac{d^2z}{dt^2} + \frac{1}{2}\left(\frac{dz}{dt}\right)^2\right] = \frac{2\gamma\cos\theta}{a} - \frac{8\mu z}{a^2}\frac{dz}{dt}, \tag{4.3}$$

where z is the height of the column, a the radius of the tube, and ρ is the density, γ the surface tension, θ the contact angle, and μ the viscosity of the liquid. By neglecting inertial terms from this equation, the classical result of Lucas [99] and

Washburn [100],

$$\frac{2\gamma\cos\theta}{a} - \frac{8\mu z}{a^2}\frac{dz}{dt} = 0, \tag{4.4}$$

is obtained. This equation describes a quasi-steady-state process where the driving capillary force is balanced by the viscous drag. Integration of this equation gives

$$z(t) = \left(\frac{a\gamma\cos\theta}{2\mu}\right)^{1/2} t^{1/2}. \tag{4.5}$$

Experiments have shown that this simple expression can also be used to describe the time evolution of capillary penetration of liquids in porous structures such as, e.g., paper [101–103].

Let us finally consider radial penetration of a wetting liquid in a porous medium. More specifically we consider radial penetration taking place from an unlimited cylindrical source of liquid with radius R_0. We start from the Darcy's law,

$$\frac{Q}{A} = -\frac{k}{\mu}\frac{\partial P}{\partial r}. \tag{4.6}$$

Here Q is the volumetric flow through a cross section of area A, k is the permeability of the medium, and P is the pressure. For the radial penetration $A = 2\pi r H$ with H the thickness of the medium. Integration of Eq. (4.6) yields

$$P_c = P(R_0) - P(R) = \frac{Q\mu}{2\pi H k}\ln\frac{R}{R_0}, \tag{4.7}$$

where P_c is the capillary pressure and R the radius of the wetted area. Now by using the average liquid velocity $V = dR/dt$, Eq. (4.7) becomes a differential equation

$$P_c = \frac{R\phi\mu}{k}\ln\left(\frac{R}{R_0}\right)\frac{dR}{dt}. \tag{4.8}$$

Integration of this equation gives

$$\left(\frac{R}{R_0}\right)^2\left(\ln\frac{R}{R_0} - \frac{1}{2}\right) + \frac{1}{2} = \frac{2kP_c}{\phi\mu R_0^2}t. \tag{4.9}$$

Capillary pressure can be written as $P_c = 2\gamma\cos\theta/a$, and different models for permeability k may be used. For example, the permeability of a system that consists of capillary tubes of radius a, is found to be $k = \phi a^2/24$. More sophisticated models of permeability of low-Reynolds-number flows through porous materials can be found in, e.g., Ref. [104]. In this case Eq. (4.9) takes the form

$$\left(\frac{R}{R_0}\right)^2\left(\ln\frac{R}{R_0} - \frac{1}{2}\right) + \frac{1}{2} = \frac{\gamma a\cos\theta}{6\mu R_0^2}t. \tag{4.10}$$

This equation resembles the one derived by Marmur for radial penetration in a single radial capillary formed between two infinite parallel plates with a cylindrical source of liquid [105]. There is, however, a different numerical constant in that case on the right-hand side of the equation. The qualitative validity of an equation of this kind for planar capillary systems was verified experimentally by Borhan and Rungta [106], and by Danino and Marmur [102].

4.2 The X-ray tomography technique

Tomography is a non-destructive and non-invasive technique used for three-dimensional imaging of materials. In X-ray tomography the sample is imaged by transmitting X rays through it. The transmitted intensity of the beam is collected with a CCD camera. This intensity is a line integral of the attenuation coefficient along the beam, and it is a function of the material composition and density. Sample is rotated and a large number of projected images is obtained by repeating the procedure at different angles. From this set of images, the local three-dimensional map of attenuation coefficients of the X rays is obtained by using the Radon transformation [107]. The quality of this reconstruction depends on the quality and number of projected images. By segmenting the grey-scale values, material components with different absorptivities for X rays can be found. For the flow simulations we need binarised images of the samples, in which the volume is divided into a pore space and a solid matrix. Recent advancements in X-ray microtomography have made imaging of such porous materials as paper possible (see e.g. Refs. [108–110]).

The results reported in this Chapter have been obtained using an X-ray tomographic image of paper obtained from Ramaswamy et al. [111] as the simulation geometry. This sample was a paper board handsheet with a basis weight of 300 $\mathrm{g/m^2}$. The voxel size of the image is $(2.0\ \mu\mathrm{m})^3$ and it has been obtained by a SkyScan-1072 device. The same sample has been previously analysed in detail by Ramaswamy et al. [111] and also flow simulations of a single-phase fluid have been done for it by the lattice-Boltzmann method [112].

4.3 Liquid penetration in paper

We used the Shan–Chen lattice-Boltzmann model to simulate capillary penetration of a wetting liquid in the X-ray microtomographic image of paper described above [I]. Parameters in the simulations were relaxation time $\tau = 1.0$, cohesion parameter $G = -0.15$, and adhesion parameter $W = -0.10$. These values result in

a wetting liquid which tends to fill the pores in paper spontaneously. Three cases were simulated: unidirectional penetration of a liquid front in the paper, radial two-dimensional penetration of liquid, and penetration of a small liquid droplet.

4.3.1 Unidirectional penetration

Unidirectional penetration of liquid in the paper sample was simulated from an unlimited liquid source that was realised by using a pressure boundary condition on one of the boundaries. We chose the value of pressure to match with the equilibrium pressure. Therefore, liquid penetrated the sample only due to the capillary forces.

Location of the liquid front was determined from the mass of the penetrated liquid, which can easily be converted to the average position of the front since the densities of both liquid and vapour phases are known as well as the porosity of the sample. Results are shown in Fig. 4.2 for penetration both in the transverse and in the in-plane directions. Results obtained are well fitted by a power law. For the exponent we found the values 0.50 and 0.47 for the transverse and in-plane directions, respectively, in good agreement with the value $1/2$ predicted by the Lucas-Washburn equation (Eq. 4.5).

All quantities in the Lucas-Washburn equation are known except the tube radius and contact angle. We can thus determine a value for the 'effective capillary radius´ $a_{eff} \equiv a\cos\theta$. In the tranverse direction we found $a_{eff} = 0.74$ μm, and in the in-plane directions 2.8 and 3.5 μm for two perpendicular directions. These results indicate that penetration in the tranverse direction is slower than in the in-plane directions. This observation is in agreement with the permeabilities obtained from single-phase lattice-Boltzmann simulations using the same tomographic image [112]. Also, the values of the effective capillary radius are in good agreement with the pore sizes obtained for the same image [111].

Results obtained are also in agreement with experiments on capillary penetration of wetting liquids in paper, which have shown that the Lucas-Washburn equation correctly describes the dynamics of the penetration process [101–103]. Notice, however, the difference in the length scales: in experiments large systems have been used whereas in our simulation penetration depths are of the order of one fibre length.

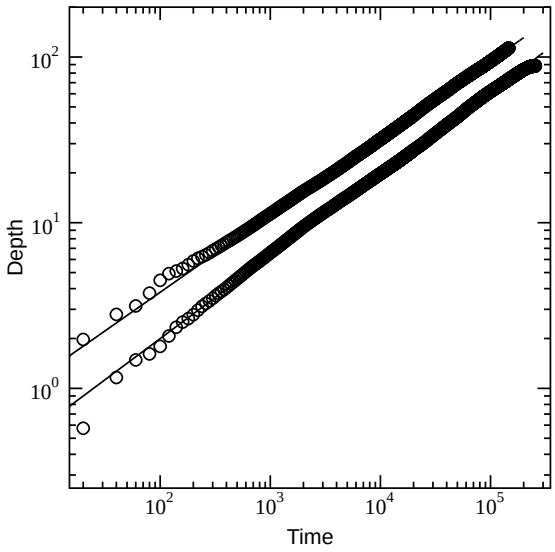

Figure 4.2: Depth of the liquid front versus time in unidirectional penetration of wetting liquid. Lower curve stands for the transverse and the upper curve for the in-plane directions. Solid lines are power-law fits to the simulation data.

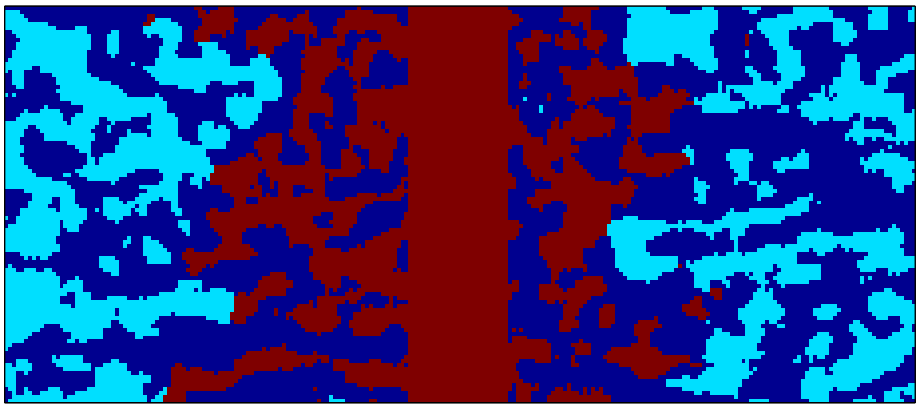

Figure 4.3: A two-dimensional cross section of radial penetration of a wetting liquid. Liquid source is located in the cavity in the middle of the sample. Blue, red, and cyan are used for solid, liquid, and vapour phases, respectively.

4.3.2 Radial penetration

The second simulated case was radial penetration of liquid from a cylindrical unlimited liquid source. Source was added to the simulation by creating a cylindrical cavity through the sample, and having the source in this cavity (see Fig. 4.3). Liquid density in the source was kept constant, and the pressure was chosen again such that penetration took place only because of capillary forces.

The position of the liquid front was obtained from the mass of penetrated liquid similarly as in the previous case. The average radius of the wetted area is shown in Fig. 4.4. The capillary model of Eq. (4.10) describing this kind of penetration was fitted to the simulation results, and good agreement was found. From the fit we could again calculate the effective capillary radius a_{eff} which was found to be 4.32 μm. The value obtained was in good agreement with the effective capillary radii obtained form unidirectional penetration in the in-plane directions of the sample.

4.3.3 Droplet penetration

The last simulation with the wetting liquid was penetration of a small droplet into the paper sample. In this case the simulation domain included in addition to the tomographic image also space for a droplet above the sample. Droplet had a diameter of about 95 lattice units, and it was positioned just above the sample. No initial velocity was given to the droplet, but it started to penetrate the sample due to capillary forces. Therefore the ratio of the inertial and capillary forces, i.e. the

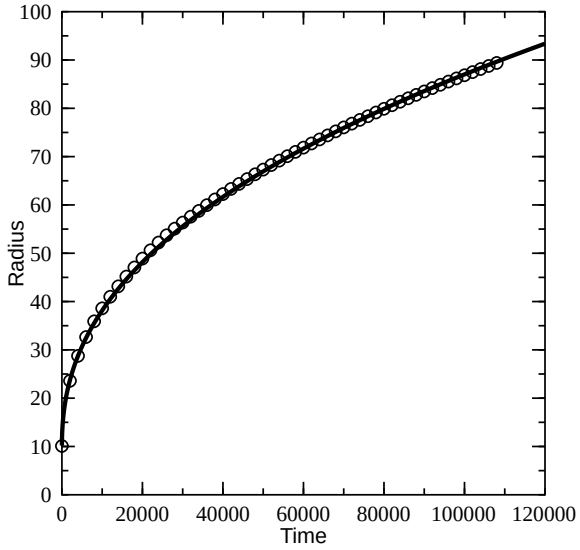

Figure 4.4: Radial penetration of wetting liquid. Simulation results are compared with Eq. (4.10)

Weber number, was small, and no splashing of the liquid occurred [113]. A droplet at four different stages of penetration is illustrated in Fig. 4.5.

The kinetics of droplet penetration was analysed by using a capillary model for two-dimensional radial penetration. The basal radius and volume of the droplet above the sample surface were determined as a function of time. Then Eq. (4.8) was numerically integrated and fitted to the simulation results so as to take into account the decreasing size of the droplet, i.e. the liquid source. Notice that only the data obtained from capillary penetration of the droplet were fitted by the model. The initial phase where droplet spreads, oscillates, and penetrates the sample mechanically was excluded. Results of the simulation and a fit by the capillary model are shown in Fig. 4.6. Simulation data are fitted well by the model. The value obtained for the effective capillary radius from droplet penetration was 16.9 μm. This is somewhat different from the value obtained from the simulation of radial penetration from an unlimited liquid source or of unidirectional penetration. One should notice, however, that the droplet used in the simulations was quite small. In principle we should construct a three-dimensional capillary model to describe the kinetics of droplet penetration. However, we noticed that droplet penetration in this paper sample was highly anisotropic. In other words, droplet penetrated mainly in the in-plane direction and only slow penetration in the transverse direction was observed. This observation is in agreements with the results we obtained

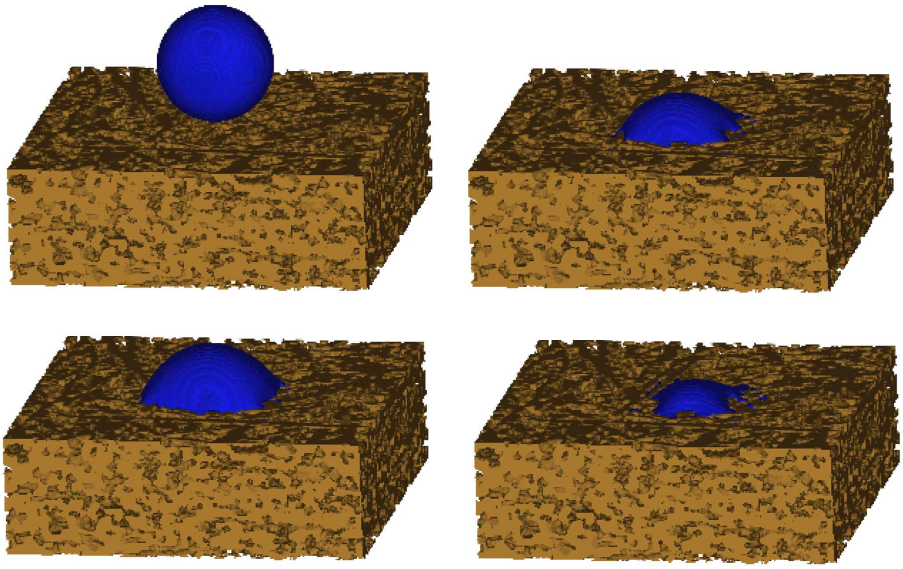

Figure 4.5: Droplet penetration. Snapshots from four different stages of the penetration process.

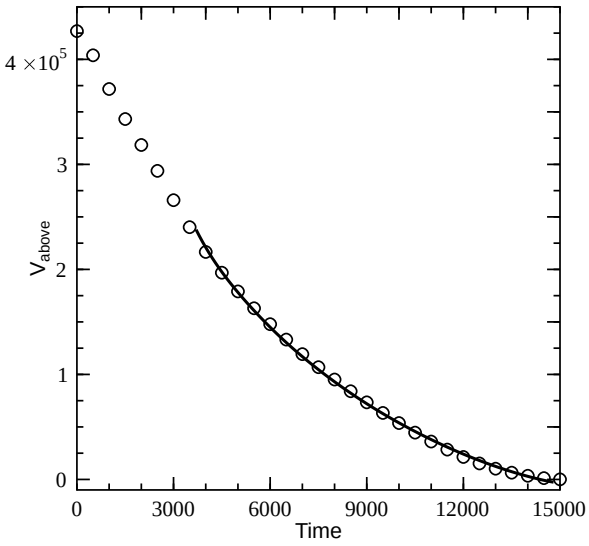

Figure 4.6: Volume of liquid above the sample shown as a function of time. Simulation results (circles) are compared with those of a capillary model (solid line).

for unidirectional penetration in the transverse and in-plane directions. Thus the assumption of two-dimensional radial penetration is not unreasonable. However, the results obtained for droplet penetration are mainly qualitative.

4.4 Intrusion of non-wetting liquid in paper

4.4.1 Background

Mercury-intrusion porosimetry is a technique that is used for characterisation of porous materials. In particular it has commonly been used for measurements of pore-size distribution. Operation of mercury-intrusion porosimetry is based on the fact that mercury is a non-wetting liquid, i.e. an external pressure is needed to force the mercury to intrude into the pores.

Interpretation of mercury intrusion data is based on the Washburn equation (Eq. (4.2)) which gives the relationship between the pressure applied to mercury and the corresponding pore size [98]. This interpretarion is based on the assumption that all the pores are cylindrical with circular cross section. All pores are also assumed to be equally accessible, i.e. connected to sample surface either directly or through larger pores. In mercury-intrusion porosimetry experiments the sample is immersed in mercury and the pressure is increased gradually. For increasing pressure mercury fills smaller and smaller pores. The intruded volume of mercury related to each pressure increment is measured and assigned with the corresponding pore size as given by the Washburn equation.

Assumptions made for the pore structure are known to be invalid for most of real materials. An example of such a situation is the so-called ink-bottle effect. The ink-bottle effect arises if a larger pore is accessible only through a smaller pore. In this case larger pore is not filled until the pressure is high enough to fill also the smaller pore. This leads to an overestimation of the volume of the small pores and to an underestimation of the volume of large pores. In 1945 Ritter and Drake published two papers where a mercury-intrusion porosimetry equipment was presented and applied to several materials [114]. These papers are the first published reports where mercury-intrusion porosimetry has been applied. Already in these papers it was pointed that "*if there exists in the material pores which are considerably larger than the largest entrances to them, these pores will be measured as of the size of the largest opening*." In other words, Ritter and Drake worried about such materials which do not fulfil the assumption of equal accessibility. The problematic pores were later named as ink-bottle pores by Meyer [115].

4.4.2 Benchmark simulations

Before discussing the actual mercury-intrusion porosimetry simulation, we consider the behaviour of non-wetting liquid, as produced by the Shan–Chen multiphase lattice-Boltzmann model, in simple pores [II]. Problems arise when the smallest pores in the tomographic images of paper have a size of just few lattice units. It is evident that in these cases discretisation is too coarse both for an accurate description of the pore structures and for the simulation method.

The first bechmark case we simulated was the intrusion of non-wetting liquid into pores of known size and shape. This test is needed because the contact angle of the liquid in Shan–Chen model cannot be directly specified. As the pore size is now known, one can use Eq. (4.2) to determine the contact angle. First we used pores with a square cross section. In this case there are no geometric discretisation errors present. Several different pore sizes were used in the simulations starting from a pore with a cross section of 5×5 ending up with a cross section of 21×21 (in lattice units). The value of the contact angle was found to be $132.8^\circ \pm 0.9^\circ$ for the adhesion strength $W = 0.05$, $116.4^\circ \pm 1.3^\circ$ for $W = 0.06$, and $153^\circ \pm 7^\circ$ for $W = 0.04$. In the first two cases the contact angle remained constant, whereas in the most non-wetting case the error bounds were quite large. This variation is related to decreased liquid density close to the pore walls due to the growing hydrophobicity, which enhances problems that results from poor discretisation.

Simulations were repeated for pores having a circular cross section. Here, especially for small (or coarsely discretised) pores, the discretised shape of the pore cross section may differ significantly from the actual shape. Therefore using Eq. (4.2) alone with the nominal radius of the pore cross section leads to an unacceptable situation where the contact angle seems to vary as a function of the nominal radius for small pore sizes. Neither does the use of hydraulic radius help the situation. The problem seems to be in the determination of the radii of small circles mapped onto a square lattice. This problem can be circumvented by taking into account the actual dicretised shape of the pore and then doing the geometric correction as explained in Ref. [II]. In Fig. 4.7 we show the result for the case $W = -0.05$. As can be seen from the figure, when the discrete shape of the pore is taken into account, contact angle corresponds very closely to the one obtained from pores with a square cross section.

As a second test case we studied the descent of a non-wetting liquid column in a capillary tube. Previously Raiskinmäki et al. have studied capillary rise dynamics by using the same lattice-Boltzmann model [46]. In this test gravity was present. The tube was initially filled by the liquid and the system was then simulated until a steady state was obtained. After this the contact angle was obtained from the

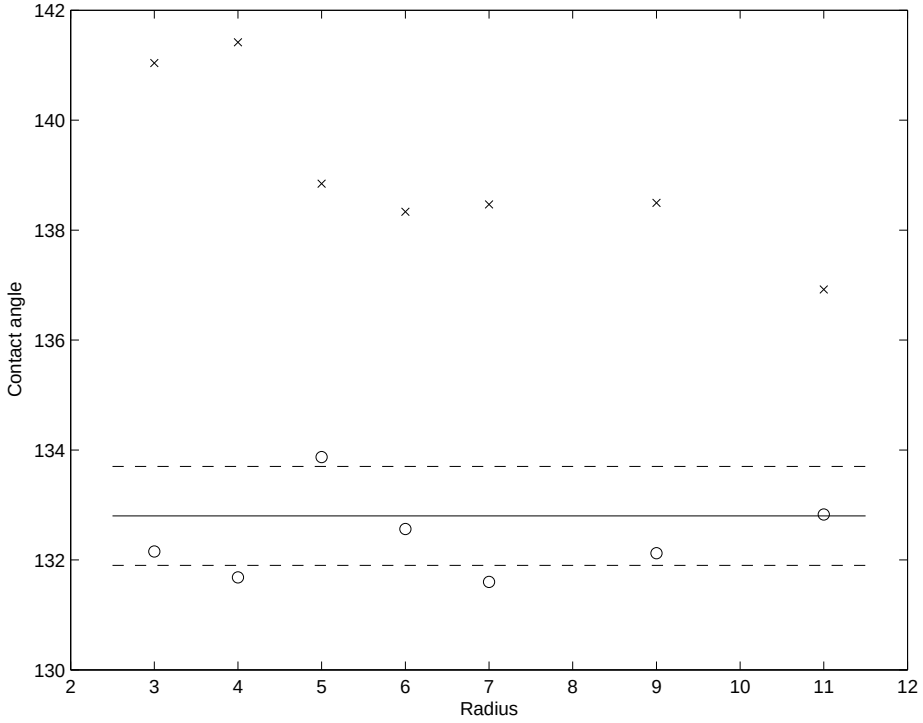

Figure 4.7: Contact angle as a function of pore radius for $W = -0.05$. Crosses indicate the values of contact angle obtained directly from Eq. (4.2) and circles the corrected values (cf. Ref. [II]). Solid line shows the contact angle obtained from pores of square cross section and dashed lines show the error bounds.

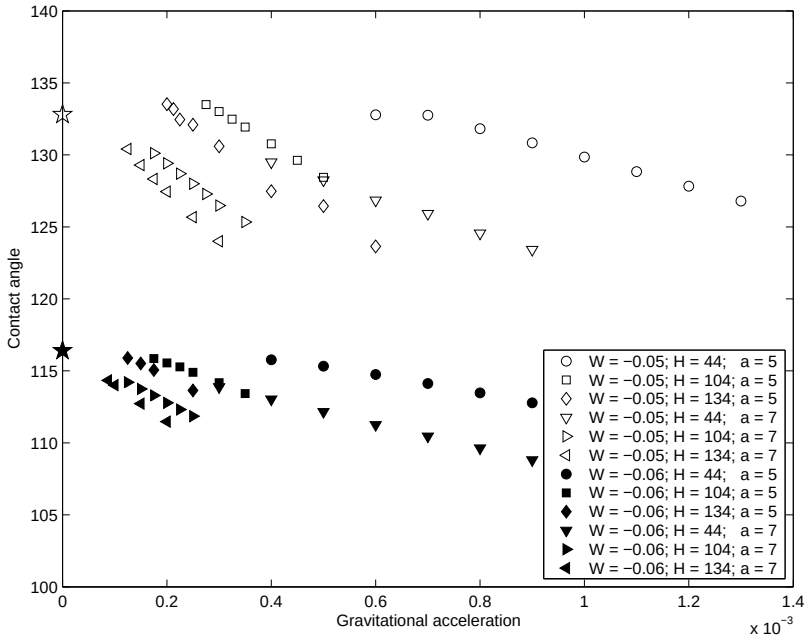

Figure 4.8: Contact angle as a function of gravitational acceleration. Stars on the vertical axis indicate the contact angles obtained from intrusion tests for $W = -0.05$ (☆) and $W = -0.06$ (★). The height of the tube is H and the size of the tube cross section is $a \times a$.

equation

$$\cos\theta = \frac{\mathcal{A}gh\Delta\rho}{\mathcal{P}\sigma}. \tag{4.11}$$

Here $\mathcal{A}$ and $\mathcal{P}$ are the area and perimeter of the pore cross section, respectively, $\Delta\rho$ is the density difference between the two phases, g the gravitational acceleration and h the height of the liquid column (negative for non-wetting liquids). As we have seen, in practice lattice-Boltzmann fluids are not totally incompressible. The effect of compressibility needs to be taken into account when gravity is present, and this was done by calculating the factor $h\Delta\rho$ as a density integral along the centreline of the tube. Results of these simulations are shown in Fig. 4.8. The contact angle determined in this way varied as the gravitational acceleration or the tube length was varied. This is most likely due to compressibility or some finite-size effects that appear in our system since the simulated system was rather small. However, the contact angle had values very close to those obtained from the pore test indicating that the values obtained from the intrusion test are reasonable.

Based on the benchmark simulation we chose to carry out the simulations by using the parameters $G = -0.15$ and $W = -0.05$. This choice adjusts the contact angle to a value that is close to the one used for paper in mercury-intrusion porosimetry experiments.

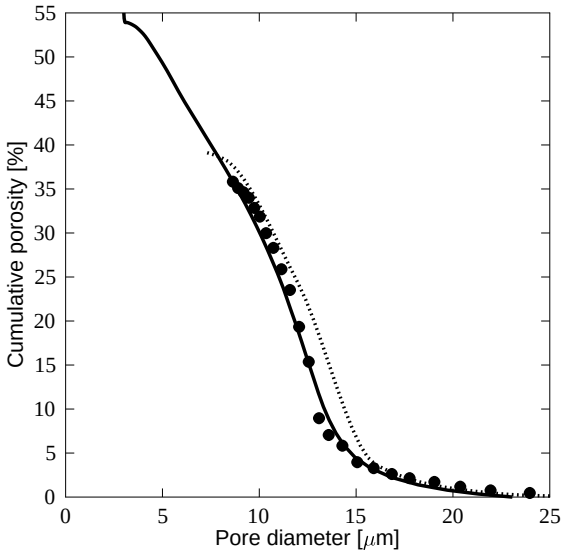

Figure 4.9: Cumulative porosities as a function of pore diameter, obtained by lattice-Boltzmann simulation (filled circles), experiment (continuous line), and invasion-percolation simulation (dotted line).

4.4.3 Intrusion of non-wetting liquid in paper

In order to clarify the role of ink-bottle pores for the results of mercury-intrusion porosimetry, we simulated by the lattice-Boltzmann method intrusion of a non-wetting liquid into an X-ray tomographic reconstruction of the sample of paper board described above [III]. The simulation results were compared with those obtained from mercury-intrusion porosimetry experiments on the same paper board [111] and a numerical invasion-percolation process in the same tomographic image. The lattice-Boltzmann simulation was made to follow the experimental procedure such that experimental results could be used to verify the simulations. Image analysis was used to obtain 'correct' pore-size and pore-throat distributions. Image analysis was also applied to situations during the simulations, thus allowing us to quantitatively analyse the intrusion process.

The pore-size analysis we used has been previously used, e.g., by Delarue et al. [116]. We chose a random initial point from the pore space. The pore size related to this point was defined as the radius of the largest sphere fitting into the pore space and including the initial point. This process was iterated to give a pore-size distribution for the pore space.

A pore-throat distribution was obtained by first determining the skeleton [117] and distance map (i.e., the distances from each pore voxel to the pore walls) of the pore space. Pore throats were found as saddle points in the distance map for the skeleton. The volume attached to each pore throat was determined as the size of the pore space that could be invaded away from the closest surface such that the pore or throat diameter remained larger than or equal to that of the initial throat.

The lattice-Boltzmann simulation followed the experimental procedure. The sample was immersed in the non-wetting liquid by adding layers of liquid on two opposite surfaces of the sample. Pressure was gradually increased and the amount of liquid intruding into the sample was measured for each increment. The obtained data were transformed into a cumulative porosity using the Washburn equation exactly in the same manner as in experiments. In Fig. 4.9 we show the cumulative porosity obtained from the simulation and compare the result with the data obtained from the experiment and image analysis. Results of simulation and experiment are surprisingly similar. Therefore, we can assume that the simulated intrusion process follows quite closely that of real intrusion.

Utilising the data obtained from these analyses we could also simulate the filling of the pore space by an invasion-percolation process. In the intrusion phase the external pressure determined the minimal pore-throat size that could be invaded, while in the extrusion phase it determined the maximum size of the pores that could be evacuated. Evacuation was only possible through a continuous liquid phase reaching the sample surface. In Fig. 4.9, we also show the result of an invasion-percolation simulation for the same sample. This simulation was affected by the discreteness of the image (pore-throat radius) more than the lattice-Boltzmann simulation, but shows, however, a qualitatively similar behaviour as the lattice-Boltzmann simulation and mercury-intrusion porosimetry measurement.

Comparing the pore spaces filled at different values of pressure (pore radius) by the lattice-Boltzmann and invasion-percolation simulations, we found that they indeed are very similar. The inflection point in the cumulative porosity gives the pressure at which the invading liquid first percolates the sample. In Fig. 4.10 we show the intruded liquid, just beyond the percolation pressure, as given by the two different simulations. It is evident that the intrusion process can quite well be described as one of invasion percolation.

This conclusion supports the earlier experimental observations in two dimensions of Ref. [118]. The result that the inflection point in the cumulative porosity gives the percolation pressure is also in line with earlier observations (see, e.g., Ref. [119]), and with earlier simulation results for a two-dimensional porous-medium model [120].

To analyse the actual intrusion process in view of the common interpretation of

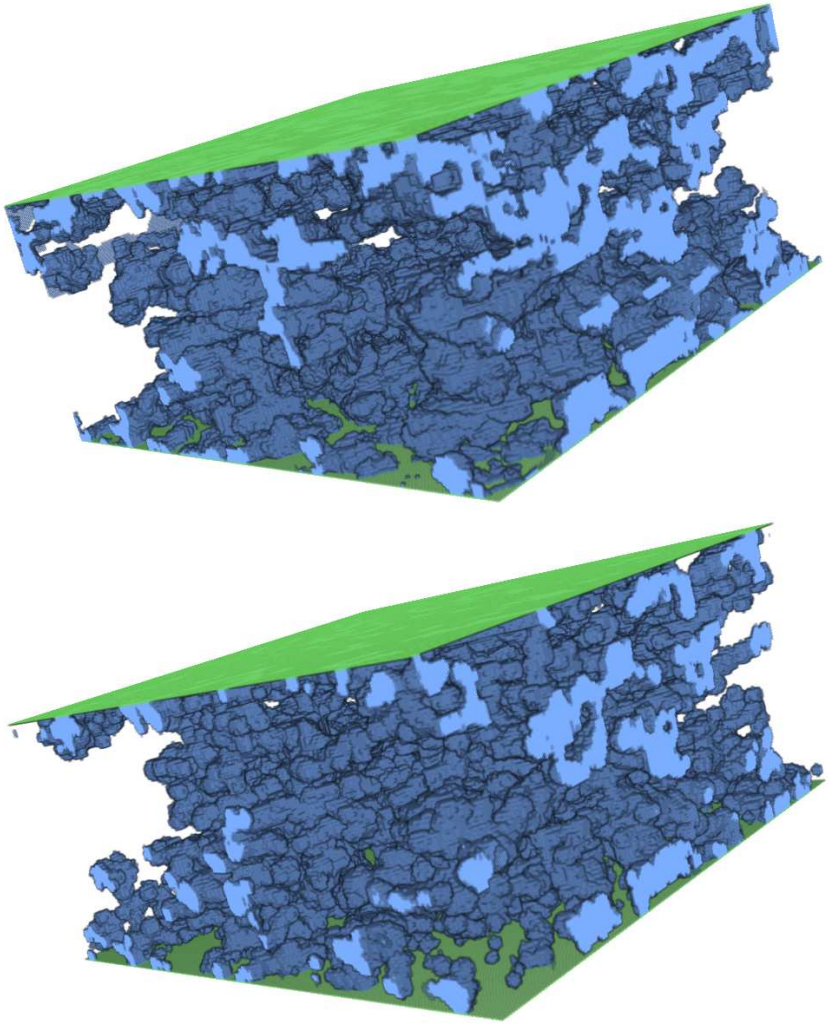

Figure 4.10: Pores filled by the liquid just beyond the percolation pressure. The upper image is the lattice-Boltzmann result and the lower one the invasion-percolation result.

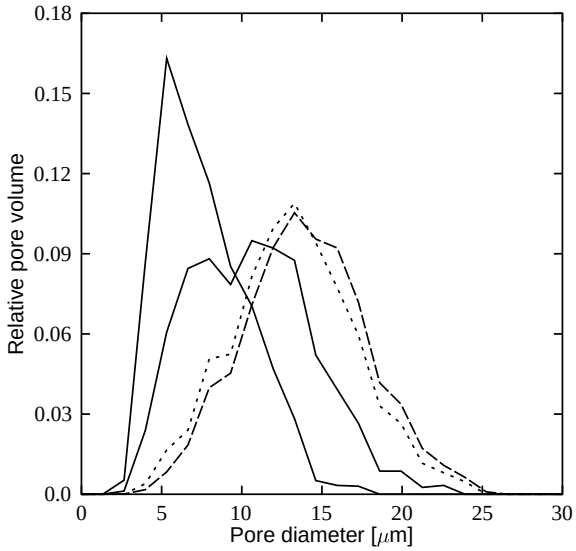

Figure 4.11: Normalised pore-size distribution of the empty part of the pore space for different values of pressure. Dashed line is the distribution just before and dotted line just after the inflection point in the cumulative porosity. Before that point the shape of the distribution does not change much, but thereafter (solid lines) increasing pressure mostly removes the largest remaining pores that remain in the distribution.

mercury-intrusion porosimetry results, by which the pore space is filled in decreasing order of pore (or pore-throat) size, we determined in the lattice-Boltzmann simulation the pore-size distributions by image analysis of the filled and empty parts of the pore space at each value of pressure. A sequence of pore-size distributions for the empty part of the pore space is shown in Fig. 4.11. Notice that their shape remains very similar even though the pressure is increased, until the inflection point in the cumulative porosity is reached. This behaviour is very different from what one expects on the basis of the common interpretation. It indicates that the ink-bottle effect is significant for paper-like porous materials, and that the access function will be markedly nonlinear.

Beyond the inflection point, the pore-size distribution of the empty pore space evolves qualitatively as expected: mainly the large-size pores gradually vanish when the pressure is increased further. Notice, however, that there is no sharp cut-off in the size of the removed pores. A similar analysis of the pore-throat distributions gave exactly the same result.

The significance of the ink-bottle effect can be evaluated by determining the access

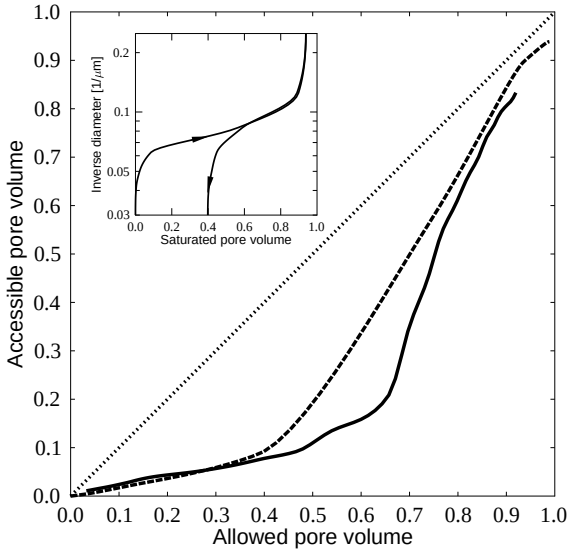

Figure 4.12: The access function for the sample of paper board as determined by lattice-Boltzmann (continuous line) and invasion-percolation (dashed line) simulations. The dotted line is the result in the absence of the ink-bottle effect. In the inset shown are the intrusion and extrusion curve for this sample as determined by invasion-percolation simulation.

function $X_a(X_{th}(p))$, where $X_{th}(p)$ is the fraction of the pore space allowed by the size of the entry pore throats at pressure p of the invading liquid [121]:

$$X_{sat}(p) = X_a(X_{th}(p)). \tag{4.12}$$

Here $X_{sat}(p)$ is the saturation curve that we have determined experimentally by mercury-intrusion porosimetry, and by the lattice-Boltzmann and invasion-percolation simulations (corresponding to the cumulative porosities of Fig. 4.9). The lattice-Boltzmann and invasion-percolation access functions are shown in Fig. 4.12. The $X_{th}(p)$ curve was determined by image analysis from the tomographic reconstruction.

As anticipated, the access function significantly deviates from the dotted line, which would be the result from equal access to all pores, i.e., without any ink-bottle effect. Notice that the lattice-Boltzmann curve lies below the invasion-percolation curve: the ink-bottle effect is somewhat underestimated by the invasion-percolation analysis that cannot completely reproduce the intrusion-extrusion process. Even then the residual saturation S_r of this process is about 0.40,

which is another indication of the significance of the ink-bottle effect in paper-like materials.

For an additional check of the consistency of the invasion-percolation picture, we also determined the residual saturation from the invasion-percolation extrusion curve. With the usual assumptions of invasion percolation [121], the residual saturation is given by

$$S_r = S_0 - \int_{r_0}^{\infty} \frac{X_a(X_{th}(r))}{X_{th}(r)} g(r) \mathrm{d}r, \tag{4.13}$$

where S_0 is the saturation at the end of intrusion, r_0 the corresponding minimum pore diameter of the filled pore space, and $g(r)$ the pore-size distribution determined from the tomographic reconstruction. If we use the lattice-Boltzmann result for the access function, we find from this equation that $S_r \approx 0.34$. This is in good agreement with the result from the invasion-percolation extrusion curve.

Our simulations show that the ink-bottle effect significantly influence the results obtained by mercury-intrusion porosimetry. After the inflection point in the cumulative porosity is reached, the intrusion process seems to be similar to what is expected. We simulated only one sample by the lattice-Boltzmann method since the simulation time was very long even though parallel computing was used. We however expect our results to be valid more generally.

Combining the lattice-Boltzmann and invasion-percolation simulations with image-analysis results, we could also show that intrusion of a non-wetting liquid can be qualitatively described by invasion-percolation process. The access function determined indicates that the ink-bottle effect is particularly important at least for paper-like materials.

5 Liquid-particle suspensions in shear flow

5.1 Suspension rheology

Rheology is, by definition [122], a science of deformation and flow. Usually rheology is described by a constitutive equation that gives the relationship between the stress and deformation in the material. In its strict meaning, definition of rheology includes everything between Hookean solids with the constitutive equation

$$\sigma = G\gamma \tag{5.1}$$

and Newtonian liquids [123] with the constitutive equation

$$\sigma = \mu\dot{\gamma}. \tag{5.2}$$

Here σ is the shear stress, γ the strain, $\dot{\gamma}$ the shear (or strain) rate, and there is shear only in one direction. Constants of proportionality, G and μ, are the elastic modulus and the viscosity, respectively. In practice, however, by rheology we understand phenomena that lie in between these two extremes [122, 124].

Liquid-particle suspensions exhibit a large variety of complex rheological behaviour [122]. If one wants to interpret rheometric measurements using the Newtonian constitutive equation, Eq. (5.2), viscosity is no more constant but depends on several factors such as the solid volume fraction and shear rate. Several predictions for the suspension viscosity as a function of solid volume fraction ϕ exist. The pioneering work was done by Einstein who derived the famous equation

$$\mu_r = \frac{\mu}{\mu_0} = 1 + 2.5\phi \tag{5.3}$$

for the relative viscosity, defined as the ratio of the viscosity of suspension to that of pure carrier liquid [125]. This equation works well for very dilute suspensions but fails to describe concentrated ones, as it neglects the effect of hydrodynamic interactions between particles. In order to take these interactions into account, higher order terms have been added to Eq. (5.3). Batchelor proposed the expression

$$\mu_r = 1 + 2.5\phi + 6.2\phi^2 \tag{5.4}$$

for the relative viscosity [126]. Batchelor's equation does not however predict viscosity correctly for suspensions with high concentration. A simple semi-empirical expression for the relative viscosity was introduced by Krieger and Dougherty [127], who proposed that

$$\mu_r = \left(1 - \frac{\phi}{\phi_{max}}\right)^{-[\eta]\phi_{max}}, \tag{5.5}$$

where ϕ_{max} is the maximum packing fraction and $[\eta]$ is the so-called intrinsic viscosity. Several values can be used for the maximum packing fraction. Experimental measurements indicate that ϕ_{max} varies between 0.63 and 0.71 corresponding to the limits of low and high values of the Peclet number (ratio of the hydrodynamic force to the Brownian force) [122]. The intrinsic viscosity is defined as

$$[\eta] = \lim_{\phi \to 0} \frac{\mu_r - 1}{\phi}. \tag{5.6}$$

For an ideal suspension with rigid and spherical particles the intrinsic viscosity is found to be 2.5 (cf. Eqs. (5.4) and (5.3)) [124]. In practice the maximum packing fraction and intrinsic viscosity are often considered as fitting parameters.

An important complex behaviour that appears in particle suspensions is shear thickening of highly concentrated suspensions. Shear thickening is observed as a rise in the viscosity when the shear rate induced in the suspension is increased. For lower solid volume fractions shear thickening in often found to be continuous, but for high concentrations close to the jamming limit shear thickening may be even discontinuous [128, 129].

Two mechanisms have been proposed to cause shear thickening. The older one, proposed by Hoffman, is based on the mechanism of order-disorder transition [130] and claims that, for low shear rates, suspension flows as ordered layers of particles and shear thickening takes place when these layers start to break up leading to a more disordered state of higher flow resistance. Based on their computer simulations with Stokesian dynamics, Brady and Bossis argued that shear thickening results from formation of particle clusters [131] which act as channels for momentum transfer through the system. Clusters, i.e. groups of particles bound together by hydrodynamic lubrication forces, bear stress efficiently thus causing the rise in the viscosity. The current understanding is that clustering is responsible for shear thickening. Although in some cases an order-disorder transition may coincide with shear thickening, there is also many examples of shear thickening occurring without an initially ordered particle configuration [128, 132, 133]. Recent two-dimensional lattice-Boltzmann simulations by Raiskinmäki et al. [87] indicate however that, for flows with a high particle Reynolds number (defined below), clustering is not able to explain the rise in the viscosity, indicating that inertial effects also play a role in shear thickening.

5.2 Suspension simulations with parallel computers

One of the main advantages of the lattice-Boltmann method is its suitability for parallel computing. The spatial locality of the updating rules, i.e. the lattice-Boltzmann equation (Eq. (3.9)), makes parallelisation of the lattice-Boltzmann method a relatively easy and straighforward task [134]. Usually one uses domain decomposition where the computational domain is divided into several subdomains. Each processor takes care of one subdomain. Information exchange is only needed between nodes at the opposite sides of the domain boundaries. The easiest way to do a domain decomposition is to divide the computational domain into (approximately) equal-sized cuboid subdomains in one, two, or three dimensions. This may lead to poor load balancing if the workload (in practice the fluid phase) is inhomogeneously distributed over the lattice. If this is the case, more sophisticated domain decomposition strategies are needed. In Ref. [135] Kandhai et al. used the orthogonal recursive bisection method to improve the parallel performance of lattice-Boltzmann simulations. Recently Wang and co-workers presented a cell-based domain-decomposition method for lattice-Boltzmann simulations, which divides the fluid cells evenly among the processors and thus provides an exact load balacing [136].

Parallelisation of a lattice-Boltzmann suspension code is a more complicated task. The main difficulty is related to the fact that particle size exceeds the lattice spacing. Since forces and torques must be integrated over the whole particle surface, the spatial locality of the lattice-Boltzmann method is lost, and parallelisation thus becomes more complicated. A particle close to a corner of a subdomain may partially be located in as many as eight different subdomains. Special care is needed to ensure that forces and torques are correctly calculated in situations of this kind, and that the good scaling behaviour of the lattice-Boltzmann method is not lost.

Our approach [IV, 137] to this parallelisation problem is to use a similar domain-decomposition strategy as usually used in single-phase lattice-Boltzmann simulations. Every processor calculates the fluid flow in the subdomain it controls and the particles are attached to processors such that the control of a particle is given to the processor that controls the subdomain where the centre point of the particle is located. If a particle is located partly in a neighbouring subdomain, its replica is send to the processor taking care of that subdomain. Every processor calculates the forces acting on all particles located completely or partially in its subdomain. After this, forces and torques of the replicas are sent to their control processors. Each processor updates the velocities, angular velocities, and positions of the paricles under its control. If in the update of particle positions a particle centre point crosses a boundary between two processors, the control of this particle is handed over to the next processor. Notice that a similar parallelisation strategy for a lattice-

Boltzmann suspension-flow solver has been used by Wolffe et al. in Ref [138].

5.3 Momentum transfer analysis in simplified suspensions

In order to understand better shear thickening and the effect of particle clusters on the viscosity of suspensions, we conducted simulations of systems consisting only of one or few particles [IV]. Suspensions were confined between parallel plates and a shear flow was achieved by moving the plates into opposite directions with equal speeds. Periodic boundary conditions were used in the other two directions.

As we discussed in Sec. 5.1, both simulations and experiments show plausible evidence that formation of particle clusters is the underlying mechanism responsible for the shear-thickening behaviour. Recent two-dimensional lattice-Boltzmann simulations by Raiskinmäki show that clustering indeed occurs simultaneously with shear thickening, but this alone is not able to explain shear thickening [139]. To this end, we studied the simplest possible suspension, i.e. a suspension consisting of only one particle confined between two parallel plates. (Notice, however, the periodic boundaries.) The system size was 50^3, and a particle with a diameter of 22 lattice units was placed in the centre of the system. System was simulated until a steady state was reached. The viscosity of the suspension was calculated from the total shear forces acting on the plates as in viscometric measurements. Simulation was repeated for several values of the particle Reynolds number

$$Re_p = \frac{\dot{\gamma} d^2}{\nu}, \tag{5.7}$$

where d is the diameter of the particle and ν is the kinematic viscosity. Reynolds number was increased by increasing the shear rate and keeping the viscosity constant. Results obtained from these simulations are shown in Fig. 5.1. A small but clear shear thickening was seen in our simulations. When repeating simulations by neglecting the nonlinear terms from the equilibrium distribution function (Eq. 3.43), i.e. simulating Stokes flow, no evidence of shear thickening was seen. This indicates that some kind of inertial effect is responsible for the shear-thickening behaviour observed. Simultaneously with shear thickening, a change in the flow field around the particle was observed. For small shear rates fluid flows around the particle, but when the shear rate increases, streamlines start to make an increasingly evident U-turn in front of the particle. Simultaneously fluid speed in the gaps between the particle and the walls relatively decreases, which furthermore causes a decrease in the (relative) angular momentum of the particle (cf. Fig. 5.1). Stress

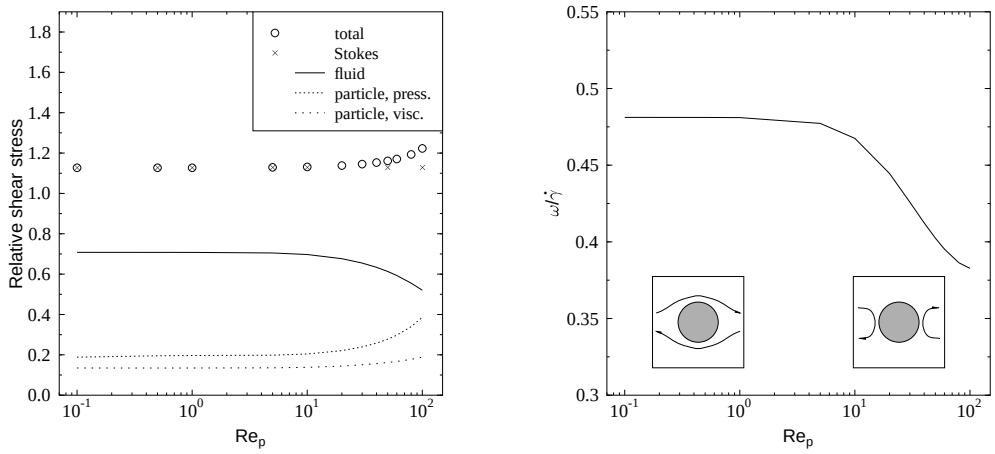

Figure 5.1: Single particle in shear flow. In the left panel shown is the relative shear stress as a function of particle Reynolds number. Also shown are results for the Stokes-flow case, and the different components of the stress in the middle plane of the system. In the right panel angular velocity of the particle is shown as a function of particle Reynolds number. The insets illustrate the change in the flow field as the shear rate increases.

analysis shows that shear thickening results from increased solid stress, in particular from the stress originating from the pressure part of the fluid stress tensor.

Although clustering alone does not seem to be able to explain the shear-thickening behaviour, it however is an important mechanism not only behind shear thickening but also in other phenomena observed in suspension flows, such as strain hardening to be discussed below in more detail. An interesting form of cluster is a chain of particles that rotates in shear flow. We studied the effect of a single artificial chain-like cluster in shear flow [IV]. This model cluster consisted of seven spherical particles with a diameter of 14 lattice units. The size of the system was $50 \times 160 \times 111$ lattice units (in the vorticity, flow, and gradient directions, respectively). As this system was sheared, the cluster rotated (see Fig. 5.2). It turned from an almost horizontal orientation to a vertical one where after the interparticle distances started to grow again and the cluster broke up. It transferred stress efficiently, which can be seen as enhanced internal stresses of the particles as well as a high shear stress of the fluid in the regions between particles (see Figs. 5.2 and 5.3). This simple simulation demonstrates the stress-transfer capability of particle clusters, which increases the viscosity of suspension as compared to randomly positioned particles in the fluid. The results discussed above are related to a low-Reynolds-number flow. We also studied the effect of shear rate on the viscosity of suspension with a single artificial cluster. We found results comparable with those for the single-particle case,

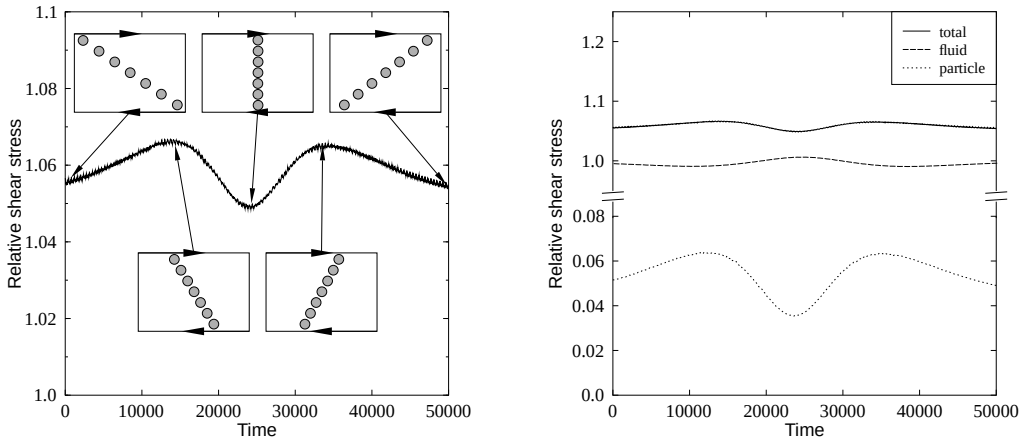

Figure 5.2: Single chain-like cluster in shear flow. In the left panel shown is the relative shear stress with changing orientation of the cluster. In the right panel this stress is divided into parts originating from the fluid stress and the internal stresses of the particle at the middle plane of the system.

i.e. for Stokes flow no shear thickening was observed whereas for Navier–Stokes flow shear thickening was found. The results shown are for a cluster at an angle with the horizontal direction of $57°$.

5.4 Strain hardening in liquid-particle suspensions

Strain hardening is an interesting phenomenon observed in many rheological materials (see e.g. Refs. [140–143]). Recently strain hardening in liquid-particle suspensions was studied in a detailed manner by Carreau and Cotton [144]. In strain hardening a significant rise in the viscosity is observed when a suspension is induced to shear. The prevailing belief is that this phenomenon is related to formation of particle clusters [144], but no direct evidence of such clustering has so far been found. One interesting feature of the strain-hardening phenomenon is that it is found even in the most simple liquid-particle suspension that consists of a Newtonian carrier liquid and non-colloidal and non-Brownian spherical particles [144]. In strain hardening some mechanisms responsible for the increased viscosity in concentrated suspensions come into operation. Therefore a detailed understanding of the underlying mechanism for strain hardening may also help us to better understand the issues related more generally to the increased viscosity in suspensions.

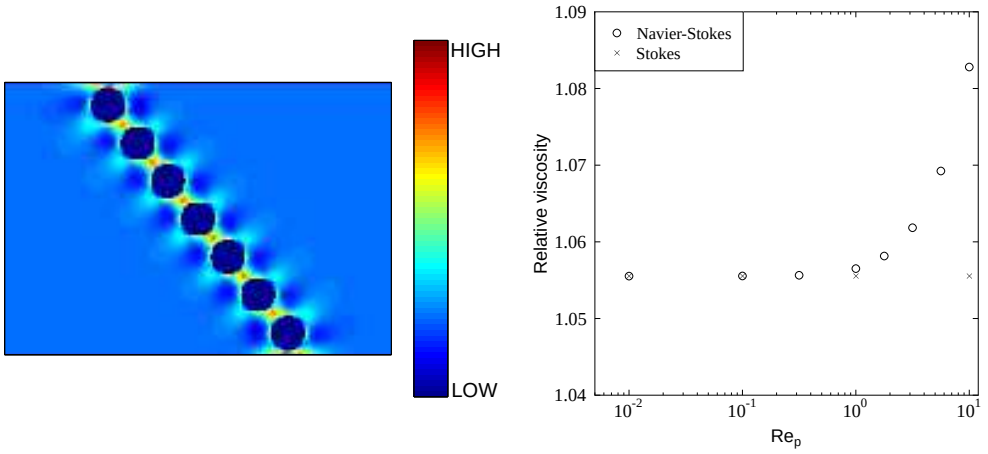

Figure 5.3: In the left panel shown is the instantaneous fluid shear stresses in the planar cross section of the system with a single cluster in a low-Reynolds-number flow. In the right panel shown is the relative viscosity as a function of particle Reynolds number for both Stokes and Navier–Stokes flows.

We investigated the strain-hardening phenomenon in liquid-particle suspensions by simulations [V]. These simulations were done in a similar plane-Couette geometry that was used above for even simpler suspensions. Size of the system in our simulations was $90 \times 260 \times 158$ lattice units (in the vorticity, flow, and gradient directions, respectively), and the suspension consisted of spherical monodispersed particles with a diameter of 12 lattice units. Four values for the solid-volume fraction were used (0.41, 0.46, 0.51, and 0.56) and the number of particles in the system varied between 1655 and 2270, respectively.

Carreau and Cotton used a procedure they called 'conditioning' in order to break the particle aggregates possibly existing initially in the suspension [144]. In conditioning a low-strain-amplitude oscillatory flow was imposed in the suspension. In simulation similar initial condition can be ensured by choosing such a particle configuration (see Fig. 5.4) in which there are no clusters.

We simulated the so-called start-up test in which shear rate was kept constant during the shearing. Simulation parameters were chosen such that the particle Reynolds number was $Re_p \approx 1.6 \cdot 10^{-2}$. In the measurements of Carreau and Cotton shear rates were significantly smaller as they varied in the interval $Re_p \sim 10^{-11} - 10^{-9}$. We could not use such low values of Re_p simply because of the restrictions set by the computational power available. We should however notice that also our simulations clearly were in the creeping flow regime. The only prob-

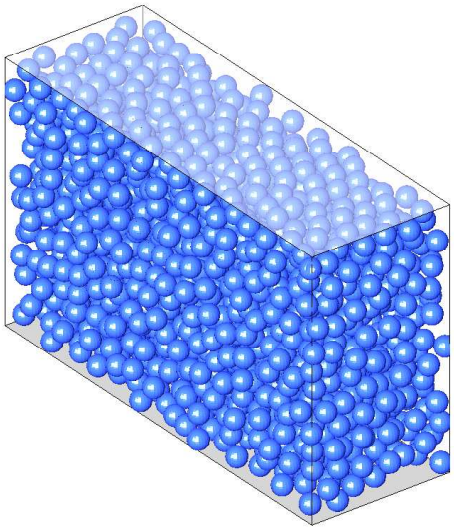

Figure 5.4: Initial particle configuration for a strain-hardening simulation with a solid-volume fraction of 0.41.

lem related to the higher value of Re_p is that in the beginning of a simulation high gradients would arise close to the moving plates causing high shear stresses on them. This would at least partially hide the strain-hardening phenomenon. To prevent this problem and to more closely comply with the experimental conditions, we initialised the simulations by holding the particles in their initial positions until a steady state was obtained. The velocities and angular velocities were however updated in a normal fashion. After the flow had developed, particles were released and the actual strain-hardening simulation started. Another difference between the experiments of Ref. [144] and our simulations was that the distance of the plates was in the experiments 100 particle diameters whereas in our simulations this distance was only 13 particle diameters. Again, perfect match between simulations and experiments would have made the computations intractable. Due to these differences we cannot expect an exact reproduction of experimental data. However, this does not prevent a qualitative comparison of the results, nor an analysis of the microstructural mechanism behind the strain-hardening phenomenon.

In Fig. 5.5 shown are viscosities as a function of strain for the four solid-volume fractions used. It is evident that simulations show a similar strain-hardening behaviour as was seen in the experiments of Ref. [144]. A rise in viscosity is observed when the strain reaches a value of approximately 0.1. For higher particle concentrations strain hardening appears at somewhat smaller strains than for lower solid-volume fractions. Also the rise in viscosity is more pronounced when the concentration in higher.

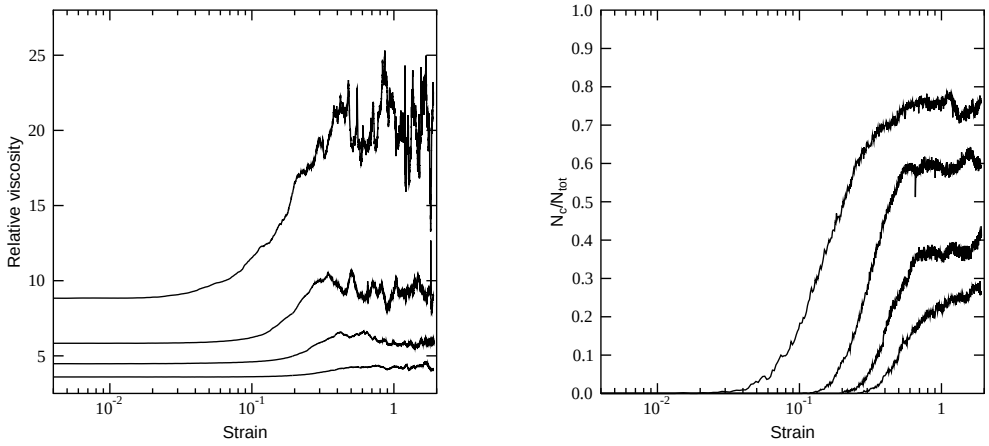

Figure 5.5: In the left panel shown is the relative viscosity as a function of strain. Highest (lowest) curve corresponds to the case with highest (lowest) solid-volume fraction. In the right panel shown is clustering as a function of strain.

Next we show that strain hardening results from formation of particle clusters. To this end we need a definition for a particle cluster. We use a simple definition where a cluster is understood as a compact group of particles where the distances of neighbouring particles are below a threshold distance δ_c. In the subsequent analysis we use the value $\delta_c = 0.1$. We define the clustering rate as the proportion of particles that belong to any of the clusters. This quantity does not completely describe the effect of clustering on the viscosity of suspension. Also the size, shape, and orientation of the clusters may affect the viscosity. The above definition of clustering should, however, give a qualitative picture of the clustering process during a start-up test.

In Fig. 5.5 shown is the clustering rate for the same simulations whose viscosities were discussed above. The behaviour of the clustering rate was quite similar to that of the viscosity. When the solid-volume fraction increased, clustering started at lower values of strain. It is evident that for higher solid-volume fractions interparticle distances decrease, which enhances clustering.

To find direct evidence of the role of particle clusters in strain hardening we studied momentum transfer through the suspension. The stresses that originate from the fluid and solid phases were determined separately. In Fig. 5.6 shown is the total viscosity and that part of the viscosity which originates from momentum transfer through the fluid. It is clear that the fluid phase does not significantly contribute to the enhanced momentum transfer observed in strain hardening and that the main

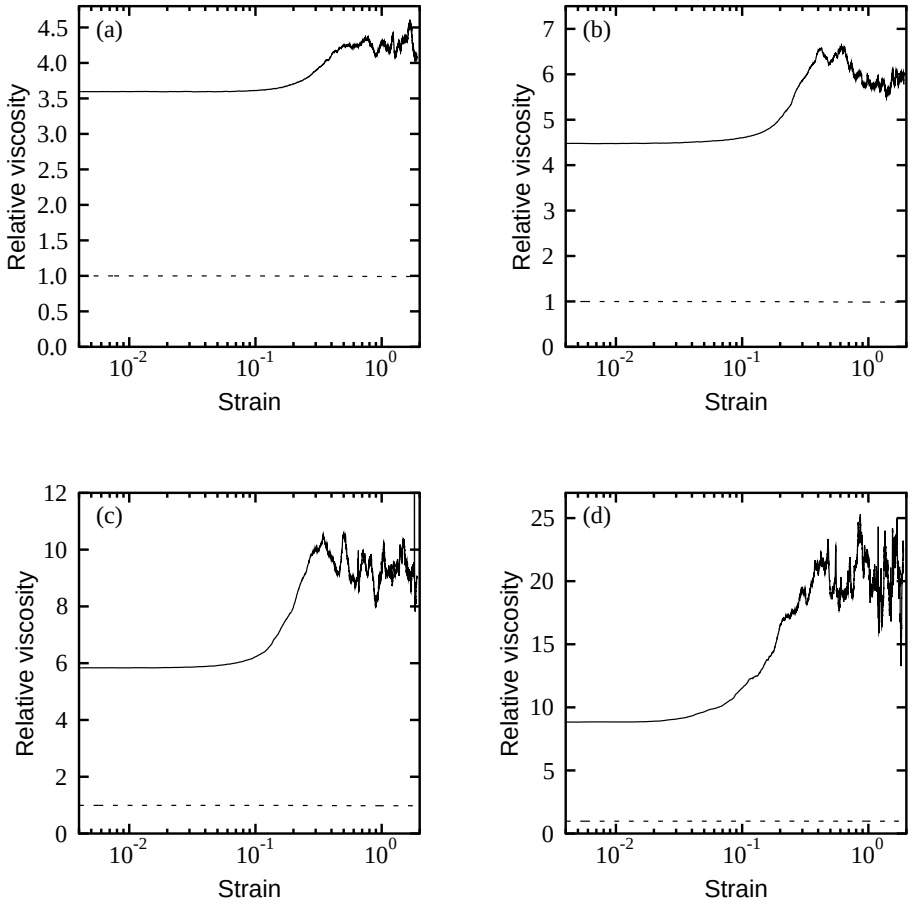

Figure 5.6: Relative viscosity as a function of strain. Dashed lines indicate the part of viscosity that originates from momentum transfer through the fluid phase. The solid-volume fraction is (a) 0.41, (b) 0.46, (c) 0.51, and (d) 0.56.

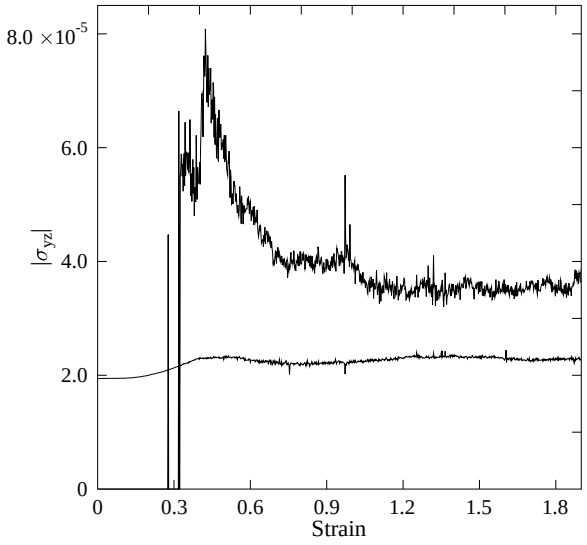

Figure 5.7: Mean internal stresses of clustered (upper curve) and non-clustered particles.

reason for strain hardening must therefore be related to the internal stresses of the particles.

We still need to show that the enhanced momentum transfer through the solid phase is dominated by the clustered particles. To this end we calculated the internal stresses of each particle in the suspension. This can be done by integrating the forces acting on the particle surfaces. The averaged components of the stress tensor of a particle are given by

$$\langle \sigma_{\alpha\beta} \rangle = \frac{1}{2V} \oint_S (P_\alpha x_\beta + P_\beta x_\alpha)\, dS, \tag{5.8}$$

where V is the volume of the particle and $\mathbf{P}$ is the external force per unit area [145]. Combining the information related to clustering and to internal stresses of particles, we can calculate the mean internal stress of clustered and non-clustered particles. Figure 5.7 shows how these stresses behave as a function of strain. We clearly see that the stresses in clustered particles are considerably higher than in non-clustered ones. Thus we can conclude that formation of particle clusters indeed is the mechanism behind strain hardening.

6 Conclusions

In this Thesis the behaviour of multiphase flows was studied with the lattice-Boltzmann method. The multiphase systems considered in this work were liquid-vapour systems in paper and liquid-particle suspensions.

The first part of the Thesis considered liquid-vapour flows in paper. High-resolution images of paper needed for the simulations were obtained with X-ray microtomography. We considered the behaviour of both wetting and non-wetting liquids in paper. For a wetting liquid we simulated spontaneous imbibition of liquid into the sample. Results were compared with capillary models that have been experimentally verified for several types of porous materials including paper. Our results were in good agreement with these models. Simulations enable investigation of imbibition at small length scales whereas experiments often measure the dynamics at larger scales. In the present simulations penetration length was approximately one fibre length. In the case of non-wetting liquid we performed a simulation that imitated a pore-size distribution measurement by mercury-intrusion porosimetry. When the data obtained from simulation was interpreted in an exactly same manner as in the experimental procedure, our results were in good agreement with those obtained from a measurement for a similar paper sample. However, when the tomographic image was analysed by image analysis, a different result was found. Since the simulation provided detailed information of the intrusion process, we were able to analyse this process by image analysis. We found that the result of mercury-intrusion porosimetry was hampered by not having equal access to all pores in the sample until the liquid first percolated the whole sample. The point of percolation corresponds to the inflection point in the cumulative porosity curve.

The second multiphase system considered was a non-Brownian and non-colloidal liquid-particle suspension induced to shear. Here our motivation was to understand the role and effect of particle clusters on the formation of viscosity in this kind of suspension. First we simulated very simple suspensions, such as that of a single particle or single chainlike particle cluster, in shear flow. A detailed momentum-transfer analysis was carried out so as to gain more information of the origin of the stress inside particles. We found that even the simplest possible suspension, namely that consisting of a single particle, exhibited shear thickening. This indicated that clustering alone cannot explain the shear thickening but also some inertial effects are involved. Also large suspensions consisting of thousands of par-

ticles were simulated. For these suspensions we studied the strain-hardening phenomenon that is observed in small-strain experiments for comparable model suspensions. In this phenomenon increased viscosity is observed when an initially immobile suspension is sheared. We found that strain hardening is caused by formation of particle clusters. These clusters efficiently transfer stress through the system, which is observed as an increased viscosity.

We have seen that lattice-Boltzmann simulations can be used as an effective tool for studying multiphase flows. These simulations are especially useful when one wants to understand the phenomena that have their origin at mesoscopic scales, and are thus difficult to investigate with experimental techniques. The large-scale simulations reported in this Thesis were done using massively parallel computing. However, the perpetually increasing computational power has made simulations with moderately large systems possible even with personal computers. To this end it seems that simulations are becoming a more and more important tool for studies on multiphase flow dynamics, and that the scales accessible by lattice-Boltzmann simulations are approaching those typical of experiments and even industrial processes.

References

[I] J. Hyväluoma, P. Raiskinmäki, A. Jäsberg, A. Koponen, M. Kataja, and J. Timonen, *Simulation of liquid penetration in paper*, Physical Review E **73**, 036705 (2006).

[II] J. Hyväluoma, P. Raiskinmäki, A. Jäsberg, A. Koponen, M. Kataja, and J. Timonen, *Evaluation of a lattice-Boltzmann method for mercury intrusion porosimetry simulations*, Future Generation Computer Systems **20**, 1003 (2004).

[III] J. Hyväluoma, T. Turpeinen, P. Raiskinmäki, A. Jäsberg, A. Koponen, M. Kataja, J. Timonen, and S. Ramaswamy, *Intrusion of non-wetting liquid in paper*, submitted for publication.

[IV] J. Hyväluoma, P. Raiskinmäki, A. Koponen, M. Kataja, and J. Timonen, *Lattice-Boltzmann simulation of particle suspensions in shear flow*, Journal of Statistical Physics **121**, 149-161 (2005).

[V] J. Hyväluoma, P. Raiskinmäki, A. Koponen, M. Kataja, and J. Timonen, *Strain hardening in liquid-particle suspensions*, Physical Review E **72**, 061402 (2005).

[1] L.D. Landau and E.M. Lifshitz, *Fluid Mechanics* (Pergamon Press, Oxford, 1975)

[2] U. Frisch, B. Hasslacher, and Y. Pomeau, Phys. Rev. Lett. **56**, 1505 (1986).

[3] P.J. Hooberbrugge and J.M.V.A. Koelman, Europhys. Lett. **19**, 155 (1992).

[4] J.J. Monaghan, Annu. Rev. Astron. Astrophys. **30**, 543 (1992).

[5] R.R. Nourgaliev, T.N. Dinh, T.G. Theofanous, and D. Joseph, Int. J. Multiphase Flow **29**, 117 (2003).

[6] J.-P. Hansen and I.R. McDonald, *Theory of simple liquids* (Elsevier Academic Press, Amsterdam, 1986).

[7] K. Huang, *Statistical Physics* (John Wiley & Sons, New York, 1967).

[8] L.E. Reichl, *A Modern Course in Statistical Physics* (John Wiley & Sons, New York, 1998).

[9] P.L. Bhatnagar, E.P. Gross, and M. Krook, Phys. Rev. **94**, 511 (1954).

[10] L.-S. Luo, Proceedings of the International Conference on Applied Computational Fluid Dynamics, Eds. J.-H. Wu and R.-J. Zhu, Beijing, China (2000), pp. 52-83.

[11] J. Hardy, Y. Pomeau, and O. de Pazzis, Phys. Rev. Lett. **31**, 276 (1973); J. Math. Phys. **14**, 1746 (1973); J. Hardy, O. de Pazzis, and Y. Pomeau, Phys. Rev. A **13**, 1949 (1976).

[12] S. Wolfram, J. Stat. Phys. **45**, 471 (1986).

[13] D. d'Humierès, P. Lallemand, and U. Frisch, Europhys. Lett. **2**, 291 (1986).

[14] G.R. McNamara and G. Zanetti, Phys. Rev. Lett. **61**, 2332 (1988).

[15] F.J. Higuera, S. Succi, and R. Benzi, Europhys. Lett. **9**, 345 (1989).

[16] F.J. Higuera and J. Jiménez, Europhys. Lett. **9**, 663 (1989).

[17] S. Succi, *The Lattice Boltzmann Equation for Fluid Dynamics and Beyond* (Oxford University Press, Oxford, 2001).

[18] S. Chen and G.D. Doolen, Annu. Rev. Fluid Mech. **30**, 329 (1998).

[19] J.M.V.A. Koelman, Europhys. Lett. **15**, 603 (1991).

[20] S. Chen, H. Chen, D.Martínez, and W. Matthaeus, Phys. Rev. Lett. **67**, 3776 (1991).

[21] Y.H. Qian, D. d'Humierès, and P. Lallemand, Europhys. Lett. **17**, 479 (1992).

[22] H. Chen, S. Chen, and W.H. Matthaeus, Phys. Rev. A **45**, R5339 (1992).

[23] D. d'Humières, in *Rarefied gas dynamics: Theory and simulations* (Eds. B.D. Shizgal and D.P. Weaver), Prog. Aeronaut. Astronaut. **159**, 450 (1992).

[24] P. Lallemand and L.-S. Luo, Phys. Rev. E **61**, 6546 (2000).

[25] D. d'Humières, I. Ginzburg, M. Krafczyk, P. Lallemand and L.-S. Luo, Phil. Trans. R. Soc. Lond A **360**, 437 (2002).

[26] A.J.C. Ladd, J. Fluid Mech **271**, 285 (1994).

[27] P.J. Dellar, J. Comput. Phys. **190**, 351 (2003).

[28] J. Latt and B. Chopard, arXiv:physics/0506157 (2005).

[29] J.D. Sterling and S. Chen, J. Comput. Phys. **123**, 196 (1996).

[30] D. Kandhai, A. Koponen, A. Hoekstra, M. Kataja, J. Timonen, and P.M.A. Sloot, J. Comput. Phys. **150**, 482 (1999).

[31] X. He and L.-S. Luo, Phys. Rev. E **55**, R6333 (1997); Phys. Rev. E **56**, 6811 (1997).

[32] X. Shan, X.-F. Yuan, and H. Chen, J. Fluid Mech. **550**, 413 (2006).

[33] R. Benzi, S. Succi, and M. Vergassola, Phys. Rep. **222**, 145 (1992).

[34] Y.-H. Qian and Y. Zhou, Europhys. Lett. **42**, 359 (1998).

[35] G. Házi and P. Kávrán, J. Phys. A: Math. Gen. **39**, 3127 (2006).

[36] A.K. Gunstensen, D.H. Rothman, S. Zaleski, and G. Zanetti, Phys. Rev. A **43**, 4320 (1991).

[37] X. Shan and H. Chen, Phys. Rev. E **47**, 1815 (1993); **49**, 2941 (1994).

[38] M.R. Swift, W.R. Osborne, and J.M. Yeomans, Phys. Rev. Lett. **75**, 830 (1995).

[39] X. He and G.D. Doolen, J. Stat. Phys. **107**, 309 (2002).

[40] L.-S. Luo, Phys. Rev. Lett. **81**, 1618 (1998); Phys. Rev. E **62**, 4982 (2000).

[41] X. He, X. Shan, and G.D. Doolen, Phys. Rev. E **57**, R13 (1998).

[42] X. He, S. Chen, and R. Zhang, J. Comput. Phys. **152**, 642 (1999); R. Zhang, X. He, and S. Chen, Comput. Phys. Commun. **129**, 121 (2000).

[43] T. Lee and C.-L. Lin, Phys. Rev. E **67**, 056703 (2003).

[44] N.S. Martys and H. Chen, Phys. Rev. E **53**, 743 (1996).

[45] M.C. Sukop and D. Or, Physica B **338**, 298 (2003); Water Resour. Res. **40**, W01509 (2004).

[46] P. Raiskinmäki, A. Shakib-Manesh, A. Jäsberg, A. Koponen, J. Merikoski, and J. Timonen, J. Stat. Phys. **107**, 143 (2002).

[47] X. Shan, Phys. Rev. E **73**, 047701 (2006).

[48] R. Benzi, L. Biferale, M. Sbragaglia, S. Succi, and F. Toschi, arXiv:nlin.CD/0602008 (2006).

[49] L. Zhu, D. Tretheway, L. Petzold, and C. Meinhart, J. Comput. Phys. **202**, 181 (2005).

[50] J. Harting, C. Kunert, and H.J. Herrmann, arXiv:physics/0509035 (2005).

[51] Q. Kang, D. Zhang, and S. Chen, Adv. Water Res. **27**, 13 (2004).

[52] S. Marconi, B. Chopard, and J. Latt, Int. J. Mod. Phys. C **14**, 1015 (2003).

[53] P. Raiskinmäki, A. Koponen, J. Merikoski, and J. Timonen, Comput. Mater. Sci. **18**, 7 (2000).

[54] R. Cornubert, D. d'Humières, and D. Levermore, Physica D **47**, 241 (1991).

[55] I. Ginzbourg and P.M. Adler, J. Phys II France **4**, 191 (1994).

[56] P. Lavallèe, J.P. Boon, and A. Noullez, Physica D **47**, 233 (1991).

[57] P.A. Skordos, Phys. Rev. E **48**, 4823 (1993).

[58] D.P. Ziegler, J. Stat. Phys. **71**, 1171 (1993).

[59] D.R. Noble, S. Chen, J.G. Georgiadis, and R.O. Buckius, Phys. Fluids **7**, 203 (1995); D.R. Noble, J.G. Georgiadis, and R.O. Buckius, J. Stat. Phys. **81**, 17 (1995).

[60] T. Inamuro, M. Yoshino, and F. Ogino, Phys. Fluids **7**, 2928 (1995); Erratum **8**, 1124 (1996); see also B. Chopard and A. Dupuis, Int. J. Mod. Phys. B **17**, 103 (2003).

[61] X. He, Q. Zou, L.-S. Luo, and M. Dembo, J. Stat. Phys. **87**, 115 (1997).

[62] A.J.C. Ladd and R. Verberg, J. Stat. Phys. **104**, 1191 (2001).

[63] C. Pan, L.-S. Luo, and C.T. Miller, Comput. Fluids, in press (2006).

[64] O. Filippova and D. Hänel, J. Comput. Phys. **147**, 219 (1998).

[65] H. Chen, C. Teixeira, and K. Molvig, Int. J. Mod. Phys. C **9**, 1281 (1998).

[66] D.R. Noble and J.C. Torczynski, Int. J. Mod. Phys. C **9**, 1189 (1998).

[67] R. Mei, L.-S. Luo, and W. Shyy, J. Comput. Phys. **155**, 307 (1999); R. Mei, W. Shyy, D. Yu, and L.-S. Luo, J. Comput. Phys. **161**, 680 (2000).

[68] R. Verberg and A.J.C. Ladd, Phys. Rev. Lett. **84**, 2148 (2000); Phys. Rev. E **65**, 016701 (2001).

[69] M. Bouzidi, M. Firdaouss, and P. Lallemand, Phys. Fluids **13**, 3452 (2001).

[70] I. Ginzburg and D. d'Humieres, Phys. Rev. E **68**, 066614 (2002).

[71] M. Rohde, D. Kandhai, J.J. Derksen, and H.E.A. Van den Akker, Phys. Rev. E **67**, 066703 (2003).

[72] M. Junk and Z. Yang, Phys. Rev. E **72**, 066701 (2005).

[73] A.J. Wagner and I. Pagonabarraga, J. Stat. Phys. **107**, 521 (2002).

[74] X. He and G. Doolen, J. Comput. Phys. **134**, 306 (1997).

[75] R. Mei, D. Yu, W. Shyy, and L.-S. Luo, Phys. Rev. E **65**, 041203 (2002).

[76] A.J.C. Ladd, Phys. Rev. Lett. **76**, 1392 (1995); A.J.C. Ladd, Phys. Rev. Lett. **88**, 048301 (2002); J. Lee and A.J.C. Ladd, Phys. Fluids **14**, 1631 (2002); N.-Q. Nguyen and A.J.C. Ladd, Phys. Rev. E **66**, 050401 (2004).

[77] C.K. Aidun and Y. Lu, J. Stat. Phys. **81**, 49 (1995); C.K. Aidun, Y. Lu, and E.-J. Ding, J. Fluid Mech. **373**, 287 (1998); E.-J. Ding and C.K. Aidun, J. Fluid Mech. **423**, 317 (2000).

[78] O. Behrend, Phys. Rev. E **52**, 1164 (1995).

[79] M.W. Heemels, M.H.J. Hagen, and C.P. Lowe, J. Comput. Phys. **164**, 48 (2000).

[80] D. Qi, J. Fluid Mech. **385**, 41 (1999); Int. J. Multiphase Flow **26**, 421 (2000); Int. J. Multiphase Flow **27**, 107 (2001); Prog. Comput. Fluid Dyn. **5**, 104 (2005); D. Qi, L. Luo, R. Aravamuthan, and W. Strieder, J. Stat. Phys. **107**, 101 (2002); D. Qi and L. Luo, Phys. Fluids **14**, 4440 (2002); J. Fluid. Mech. **477**, 201 (2003).

[81] Z.-G. Feng and E.E. Michaelides, Phys. Fluids **14**, 49 (2002); Int. J. Multiphase Flow **28**, 479 (2002); J. Hydr. Engin. **129**, 985 (2003); Int. J. Multiphase Flow **29**, 943 (2003).

[82] C. Migliorini, Y.H. Qian, H. Chen, E.B. Brown, R.K. Jain, and L.L. Munn, Biophys. J. **83**, 1834 (2002); C. Sun, C. Migliorini, and L.L. Munn, Biophys. J. **85**, 208 (2003); C. Sun and L.L. Munn, Biophys. J. **88**, 1635 (2005).

[83] H. Li, H. Fang, Z. Lin, S. Xu, and S. Chen, Phys. Rev. E **69**, 031919 (2004); H.-B. Li, X.-Y. Lu, H.-P. Fang, Z.-F. Lin, Prog. Comput. Fluid Dyn. **5**, 65 (2005).

[84] M.E. Cates, K. Stratford, R. Adhikari, P. Stansell, J.-C. Desplat, I. Pagonabarraga, and A.J. Wagner, J. Phys.: Condens. Matter **16**, S3903 (2004); K. Stratford, R. Adhikari, I. Pagonabarraga, and J.-C. Desplat, J. Stat. Phys. **121**, 163 (2005); M.E. Cates, R. Adhikari, and K. Stratford, J. Phys.: Condens. Matter **17**, S2771 (2005); K. Stratford, R. Adhikari, I. Pagonabarraga, J.-C. Desplat, and M.E. Cates, Science **309**, 2198 (2005).

[85] J. Kromkamp, D.T.M. van den Ende, D. Kandhai, R.G.M. van der Sman, and R.M. Boom, J. Fluid Mech. **529**, 253 (2005); Chem. Eng. Sci. **61**, 858 (2006).

[86] P. Raiskinmäki, A. Shakib-Manesh, A. Koponen, A. Jäsberg, M. Kataja, and J. Timonen, Comput. Phys. Commun. **129**, 185 (2000); A. Shakib-Manesh, P. Raiskinmäki, A. Koponen, M. Kataja, and J. Timonen, J. Stat. Phys. **107**, 67 (2002); A. Shakib-Manesh, J.A. Åström, A. Koponen, P. Raiskinmäki, and J. Timonen, Eur. Phys. J. E **9**, 97 (2002).

[87] P. Raiskinmäki, J.A. Åström, M. Kataja, M. Latva-Kokko, A. Koponen, A. Jäsberg, A. Shakib-Manesh, and J. Timonen, Phys. Rev. E **68**, 061403 (2003).

[88] Z.-G. Feng and E.E. Michaelides, J. Comput. Phys. **195**, 602 (2004); **202**, 20 (2005).

[89] A. ten Cate, J.J. Derksen, L.M. Portela, and H.E.A. van den Akker, J. Fluid Mech. **519**, 233 (2004).

[90] A. Chatterji and J. Horbach, J. Chem. Phys. **122**, 184903 (2005).

[91] A. Masselot and B. Chopard, Europhys. Lett. **42**, 259 (1998); B. Chopard, A. Masselot, and A. Dupuis, Comput. Phys. Commun. **129**, 167 (2000); A. Dupuis and B. Chopard, J. Comput. Phys. **178**, 161 (2002).

[92] R.M.H. Merks, A.G. Hoekstra, and P.M.A. Sloot, J. Comput. Phys. **183**, 563 (2002).

[93] J. Kromkamp, A. Bastiaanse, J. Swarts, G. Brans, R.G.M. van der Sman, and R.M. Boom, J. Membr. Sci. **253**, 67 (2005).

[94] M.P. Allen and D.J. Tildesley, *Computer Simulation of Liquids* (Clarendon Press, Oxford, 1987).

[95] N.-Q. Nguyen and A.J.C. Ladd, Phys. Rev. E **66**, 046708 (2002).

[96] E.-J. Ding and C.K. Aidun, J. Stat. Phys. **112**, 685 (2003).

[97] P.G. de Gennes, Rev. Mod. Phys. **57**, 827 (1985).

[98] E.W. Washburn, Proc. Natl. Acad. Sci. **7**, 115 (1921).

[99] R. Lucas, Kolloid Z. **23**, 15 (1918).

[100] E.W. Washburn, Phys. Rev. **17**, 273 (1921).

[101] R. Williams, J. Colloid Interface Sci. **79**, 287 (1981).

[102] D. Danino and A. Marmur, J. Colloid Interface Sci. **166**, 245 (1994).

[103] J. Bico and D. Quéré, Europhys. Lett. **61**, 348 (2003).

[104] G.W. Jackson and D.F. James, Can. J. Chem. Eng. **64**, 364 (1986).

[105] A. Marmur, J. Colloid Interface Sci. **124**, 301 (1988).

[106] A. Borhan and K.K. Rungta, J. Colloid Interface Sci. **158**, 403 (1993).

[107] F. Natterer, *The Mathematics of Computerized Tomography* (SIAM, Philadelphia, 2001).

[108] E.J. Samuelsen, P.-J. Houen, Ø.W. Gregersen, T. Helle, and C. Raven, Proceedings of Tappi International Paper Physics Conference (1999), pp. 307-312.

[109] T.E. Gureyev, R. Evans, A.W. Stevenson, D. Gao, and S.W. Wilkins, Tappi J. **84**, 52 (2001).

[110] A. Goel, M. Tzanakakis, S. Huang, S. Ramaswamy, W.S. Hu, D. Choi, and B.V. Ramarao, Tappi J. **84**, 1 (2001).

[111] S. Ramaswamy, S. Huang, A. Goel, A. Cooper, D. Choi, A. Bandyopadhyay, and B. V. Ramarao, Proceedings of the 12th Fundamental Research Symposium on the Science of Papermaking, Pulp and Paper Fundamental Research Society, Bury, Lancashire, UK, 2001, pp. 1289-1311.

[112] U. Aaltosalmi, M. Kataja, A. Koponen, J. Timonen, A. Goel, G. Lee, and S. Ramaswamy, J. Pulp Paper Sci. **30**, 251 (2004).

[113] K. Range and F. Feuillebois, J. Colloid Interface Sci. **203**, 16 (1998).

[114] H.L. Ritter and L.C. Drake, Ind. Eng. Chem. **17**, 782 (1945); **17**, 787 (1945).

[115] H.I. Meyer, J. Appl. Phys. **24**, 510 (1952).

[116] J.F. Delarue, E. Perrier, Z.Y. Yu, and B. Velde, J. Phys. Chem. Earth **24**, 639 (1999).

[117] K. Palgyi and A. Kuba, Pattern Recognition Lett. **19**, 613 (1998).

[118] J.-D. Chen and J. Koplik, J. Colloid Interface Sci. **108**, 304 (1985).

[119] A.J. Katz and A.H. Thompson, Phys. Rev. B **34**, 8179 (1986).

[120] E.J. Garboczi and D.J. Bentz, Ceramics Transactions **16**, 265 (1991).

[121] R.G. Larson and N. R. Morrow, Powder Tech. **30**, 123 (1981).

[122] H.A. Barnes, J.F. Hutton, and K. Walters, *An Introduction to Rheology* (Elsevier Science Publishers, Amsterdam, 1989).

[123] I. Newton, *The Principia: Mathematical Principles of Natural Philosophy*, translation by I.B. Cohen and A. Whitman (University of California Press, Berkeley, 1999).

[124] Ch.W. Macosko, *Rheology: Principles, Measurements, and Applications* (Wiley-VCH, New York, 1994).

[125] A. Einstein, Ann. Phys. **19**, 289 (1906); **34**, 591 (1911).

[126] G.K. Batchelor, J. Fluid Mech. **83**, 97 (1977).

[127] I.M. Krieger and T.J. Dougherty, Trans. Soc. Rheol. **3**, 137 (1959).

[128] H.M. Laun, R. Bung, S. Hess, W. Loose, O. Hess, K. Hahn, E. Hädicke, R. Hingmann, F. Schmidt, and P. Lindnew, J. Rheol. **36**, 743 (1992).

[129] P. d'Haene, J. Mewis, and G.G. Fuller, J. Colloid Interface Sci. **156**, 350 (1993).

[130] R.L. Hoffman, Trans. Soc. Rheol. **16**, 155 (1972); J. Colloid Interface Sci. **46**, 491 (1974).

[131] J.F. Brady and G. Bossis, J. Fluid Mech. **155**, 105 (1985).

[132] J. Bender and N.J. Wagner, J. Rheol. **40**, 899 (1996).

[133] J.R. Melrose, J.H. van Vliet, and R.C. Ball, Phys. Rev. Lett. **77**, 4660 (1996).

[134] G. Punzo, F. Massaioli, and S. Succi, Comput. Phys. **8**, 705 (1994).

[135] D. Kandhai, A. Koponen, A.G. Hoekstra, M. Kataja, J. Timonen, and P.M.A. Sloot, Comput. Phys. Commun. **111**, 14 (1998).

[136] J. Wang, X. Zhang, A.G. Bengough, and J.W. Crawford, Phys. Rev. E **72**, 016706 (2005).

[137] T. Suviola, Proceedings of PARA 2002, June 15 - 18, 2002, Espoo, Finland, J. Fagerholm et al. (eds.), Lecture Notes in Computer Science **2367**, 603-610 (2002).

[138] G. Wolffe, J. Oleszkiewicz, D. Cherba, and D. Qi, Proceedings of PDPTA '02, June 24-27, 2002, Las Vegas, USA, H.R. Arabnia (ed.), CSREA Press, pp. 2016-2022.

[139] P. Raiskinmäki, *Dynamics of multiphase flows: liquid-particle suspensions and droplet spreading*, PhD Thesis, University of Jyväskylä (2004).

[140] F. Gadala-Maria and A. Acrivos, J. Rheol. **24**, 799 (1980).

[141] L. Levitt and C.W. Macosko, J. Rheol. **41**, 671 (1997).

[142] K. Autio, L. Flander, R. Heinonen, and A. Kinnunen, Cereal Chem. **76**, 912 (1999).

[143] G.P. Citerne, P.J. Carreau, and M. Moan, Rheol. Acta **40**, 86 (2001).

[144] P.J. Carreau and F. Cotton, in *Transport properties in bubbles, drops, and particles*, Second edition, D. De Kee, R.P. Chhabra (eds.), (Taylor & Francis, New York, 2002) pp. 397-425.

[145] L.D. Landau and E.M. Lifshitz, *Theory of Elasticity*, Second English Edition (Pergamon Press, Oxford, 1970).